



Novel Atmospheric Dynamics Shape the Inner Edge of the Habitable Zone around White Dwarfs

Ruizhi Zhan^{ID}, Daniel D. B. Koll^{ID}, and Feng Ding^{ID}

Dept. of Atmospheric and Oceanic Sciences, School of Physics, Peking University, Beijing 100871, People's Republic of China; dkoll@pku.edu.cn

Received 2024 April 8; revised 2024 May 31; accepted 2024 June 4; published 2024 August 12

Abstract

White dwarfs offer a unique opportunity to search nearby stellar systems for signs of life, but the habitable zone around these stars is still poorly understood. Since white dwarfs are compact stars with low luminosity, any planets in their habitable zone should be tidally locked, like planets around M dwarfs. Unlike planets around M dwarfs, however, habitable white dwarf planets have to rotate very rapidly, with orbital periods ranging from hours to several days. Here we use the ExoCAM global climate model to investigate the inner edge of the habitable zone around white dwarfs. Our simulations show habitable planets with ultrashort orbital periods ($P \lesssim 1$ day) enter a “bat rotation” regime, which differs from typical atmospheric circulation regimes around M dwarfs. Bat rotators feature mean equatorial subrotation and a displacement of the surface’s hottest regions from the equator toward the midlatitudes. We qualitatively explain the onset of bat rotation using shallow water theory. The resulting circulation shifts increase the dayside cloud cover and decrease the stratospheric water vapor, expanding the white dwarf habitable zone by $\sim 50\%$ compared to estimates based on 1D models. The James Webb Space Telescope should be able to quickly characterize bat rotators around nearby white dwarfs thanks to their distinct thermal phase curves. Our work underlines that tidally locked planets on ultrashort orbits may exhibit unique atmospheric dynamics, and guides future habitability studies of white dwarf systems.

Unified Astronomy Thesaurus concepts: Astrobiology (74); Exoplanet atmospheres (487); Atmospheric dynamics (2300); Extrasolar rocky planets (511); White dwarf stars (1799); Habitable planets (695); Habitable zone (696)

1. Introduction

Searching for potential signs of life outside the solar system is one of the main challenges of modern astronomy. By 2024 April, there were more than 5600 confirmed exoplanets.¹ Most of these planets orbit main-sequence stars, such as Sun-like G dwarfs or smaller M dwarfs. Some of them also orbit inside their star’s habitable zone and have the right size to potentially sustain life. Nevertheless, the search for biosignatures remains inconclusive. This is largely because transmission spectroscopy, the most promising method for detecting biosignatures, strongly depends on the ratio between the planet and stellar radius. Earth-sized planets are all much smaller than main-sequence stars, which is why even optimistic estimates suggest that searching these planets for biosignatures will require major observational effort involving tens to hundreds of repeated transits (Morley et al. 2017; Lustig-Yaeger et al. 2019; Meadows et al. 2023).

In this context, habitable planets around white dwarfs offer a unique opportunity (Agol 2011; Barnes & Heller 2013; Cortes & Kipping 2019; Kaltenegger et al. 2020; Kozakis et al. 2020). White dwarfs are small, with radii approximately equal to Earth’s, so planets orbiting these stars are much easier to characterize via transmission spectroscopy. Previous estimates suggest that, for a suitable white dwarf system, the James Webb Space Telescope (JWST) might be able to detect a biosignature gas like CH₄ in a single transit (Lin et al. 2022). Similarly, JWST should be able to

detect stratospheric clouds on an Earth-sized planet inside a white dwarf’s habitable zone within just four transits (Doshi et al. 2022).

To date there are no known habitable white dwarf planets. Nevertheless, multiple reasons suggest such planets could exist. First, white dwarfs are common and make up about 5% of nearby stars, which means they are about as abundant as Sun-like G dwarfs (Golovin et al. 2023). Second, several nonhabitable white dwarf planets have already been detected (Veras 2021), including the transiting gas giant WD 1856+534 b (Vanderburg et al. 2020). Third, although a star’s habitable planets should be destroyed when the star leaves the main sequence and becomes a white dwarf, there are multiple ways to reform habitable planets. About half of all white dwarfs are polluted or have circumstellar disks (Koester et al. 2014; Putirka & Xu 2021; Farihi et al. 2022), indicating many of them may be actively forming planets (Farihi 2016). Distant planets, which survive the transition of their host star into a white dwarf, can also migrate inward (Veras & Gaensicke 2015; Muñoz & Petrovich 2020; O’Connor et al. 2020), making it possible for these bodies to end up in the habitable zone.

Should white dwarfs indeed support habitable planets, they might end up providing the final refuge for life on galactic timescales. About 97% of stars, including the Sun, will evolve into white dwarfs after the main sequence (Fontaine et al. 2001). White dwarfs are born hot, with effective temperatures of 10^5 – 10^4 K, but cool rapidly via neutrino emission and thermal radiation. After cooling below 20,000–10,000 K, white dwarfs stop emitting neutrinos and their cooling process slows down (Fontaine et al. 2001; Bédard et al. 2020). Previous studies suggested that white dwarf systems can then remain habitable over timescales of 1–10 Gyr, with a habitable zone that slowly shrinks as the star cools (Agol 2011; Becker et al. 2023), which is opposite to their main-sequence progenitors.

¹ <https://exoplanets.nasa.gov>

However, previous studies of white dwarf systems were based on idealized energy-balance models or 1D radiative–convective atmospheric models, and so did not account for atmospheric dynamics. The gold standard for habitability calculations are 3D global climate models (GCMs), which self-consistently resolve the interaction between atmospheric dynamics, radiation, clouds, and ocean dynamics (Yang et al. 2013, 2023; Wolf & Toon 2014; Hu & Yang 2014; Kopparapu et al. 2016; Noda et al. 2017; Fujii et al. 2017; Komacek & Abbot 2019; Del Genio et al. 2019; Turbet et al. 2022). Habitable zone calculations of M dwarfs show that GCMs tend to predict significantly wider habitable zones than 1D models, which considerably increases the inferred frequency of habitable planets around main-sequence stars (Yang et al. 2013, 2023; Wolf & Toon 2014; Kopparapu et al. 2016; Noda et al. 2017; Fujii et al. 2017; Komacek & Abbot 2019; Turbet et al. 2022). In contrast, the impact of atmospheric dynamics on the white dwarf habitable zone is still unclear.

Like M dwarf planets, white dwarf planets should be tidally locked into synchronous rotation. Unlike M dwarfs, whose habitable zone corresponds to orbital periods of $\mathcal{O}(10)$ days, the habitable zone of white dwarfs corresponds to orbital periods as short as 2 hr. Only a few GCM studies have considered tidally locked habitable planets with such rapid rotation rates, and these studies suggest that white dwarf planets might differ strongly from M dwarf planets (Merlis & Schneider 2010; Noda et al. 2017; Penn & Vallis 2018; Haqq-Misra et al. 2018; Komacek & Abbot 2019; Cohen et al. 2024). For example, Haqq-Misra et al. (2018) showed that habitable M dwarf planets fall into three dynamical regimes: slow rotation (roughly, orbital periods of $P > 20$ days), Rhines rotation (5 days $< P < 20$ days), and rapid rotation ($P < 5$ days). These regimes are associated with large differences in winds, heat transport, and cloud cover, modifying the M dwarf habitable zone. Similarly, Noda et al. (2017) investigated the impact of rotation on synchronously rotating planets and found that the atmospheric circulation changes strongly and abruptly at $P \sim 1$ day.

In this paper we therefore investigate the inner edge of the habitable zone around white dwarfs using a 3D GCM. We report a novel dynamical regime, the “bat rotation” regime, for planets with ultrashort orbital periods ($P \lesssim 1$ day) and investigate how it affects the inner edge of the habitable zone. Section 2 describes the model and the assumed stellar and planetary parameters. Section 3 presents the bat rotation regime, compares it to other dynamical regimes of tidally locked planets, and uses shallow water theory to explain why the onset of bat rotation happens at $P \sim 1$ day. Section 4 shows that the bat rotation regime widens the habitable zone, by increasing dayside cloud cover and drying out the stratosphere; these effects push the runaway greenhouse limit (RGHL) closer to the star and also suppress the moist greenhouse. Section 5 expands beyond the inner edge of the habitable zone to show that most habitable planets around white dwarfs are likely to be bat rotators; it also discusses how our theoretical predictions can be tested using thermal phase curves with JWST. Finally, the paper concludes in Section 6.

2. Methods and Model

2.1. Stellar Configuration

For the white dwarf host stars in our simulations, we used the most probable parameters based on Gaia EDR2 and EDR3

(Jiménez-Esteban et al. 2018; Fusillo et al. 2021). White dwarfs are assumed to be type DA (pure H envelope) with effective temperatures in the range $3500 \leq T_{\text{eff}} [\text{K}] \leq 10,000$. For white dwarfs at 5000 K, 8000 K, and 10,000 K we use the default stellar spectra from ExoCAM.² ExoCAM does not provide white dwarf spectra at 3500 K and 6500 K, so for those stars we use spectral energy distributions (SEDs) based on 3D non-LTE models from Tremblay et al. (2013, 2015).³ Note that the choice of stellar SED affects the modeled climates. Sensitivity tests show that, for the same stellar effective temperature, SEDs based on the 3D non-LTE models from Tremblay et al. (2013, 2015) lead to somewhat higher surface temperatures than the default ExoCAM spectra (see Appendix A.1).

All white dwarfs are assumed to have the same mass, $M = 0.6 M_{\odot}$, and radius, $a = 0.012 a_{\odot}$. These values are based on the mass–radius relationship $a_{\text{WD}}/a_{\odot} \approx 0.0127 (M_{\text{WD}}/M_{\odot})^{-1/3} \sqrt{1 - 0.607(M_{\text{WD}}/M_{\odot})^{4/3}}$ from Veras (2016). Here a and M are radius and mass, while subscript WD and \odot represent the white dwarf and the Sun, respectively. The surface gravity of a white dwarf with $0.6 M_{\odot}$ is $\log(g[\text{cm s}^{-2}]) = 8$.

2.2. Planetary Configuration

To compare our results with previous habitable zone calculations for M dwarfs, we use the same model assumptions and parameters as in previous studies (e.g., Yang et al. 2014; Kopparapu et al. 2016, 2017). We assume a planet with the same radius, mass, and surface gravity as Earth. For the planet’s surface we assume an aqua-planet without land and a 50 m deep slab ocean (discussed in more detail in Section 2.3). The atmosphere consists of only N_2 and H_2O . The orbital period P is equal to

$$P = 365.25 \text{ days} \left(\frac{M_{\odot}}{M_{\text{WD}}} \right)^{\frac{1}{2}} \left(\frac{T_{\text{WD}}}{T_{\odot}} \right)^3 \times \left(\frac{a_{\text{WD}}}{a_{\odot}} \right)^{\frac{3}{2}} \left(\frac{F_{\oplus}}{F_{\text{p}}} \right)^{\frac{3}{4}}, \quad (1)$$

which is derived from Kepler’s third law. In Equation (1), M is the stellar mass, T is the stellar effective temperature, a is the stellar radius, and F is the flux received by the planet. The subscripts \odot , \oplus , WD, and p represent the Sun, Earth, white dwarf, and the planet orbiting the white dwarf, respectively.

In our simulations, P lies in the range of $3 \text{ hr} < P < 3.4 \text{ days}$. With such a short P and corresponding small semimajor axes, the timescales for tidal circularization and tidal locking around white dwarfs are less than 1000 yr (Agol 2011). This is much shorter than the duration of the habitable zone, so we assume all planets are 1:1 tidally locked with zero obliquity and eccentricity. In addition we assume the planet is solely heated by the host star; other energy sources such as tidal and geothermal heating (Becker et al. 2023) are not included. Tidal heating requires non-orbital eccentricity or a non-tidally locked rotation state, so ignoring its effect is consistent with the assumed orbit and rotation state.

² White dwarf spectra from ExoCAM: <https://github.com/storyofthewolf/ExoRT/tree/main/data/solar>.

³ White dwarf spectra from 3D non-LTE model: <https://warwick.ac.uk/fac/sci/physics/research/astro/people/tremblay/modelgrids>.

2.3. Three-dimensional Global Climate Model

The climate simulations use ExoCAM⁴ (Wolf et al. 2022), a 3D GCM modified from the Community Atmosphere Model version 4 (Neale et al. 2010). ExoCAM uses ExoRT, a correlated-k radiative transfer package which employs the HITRAN 2016 database (Gordon et al. 2017).

For the planet's surface we assume an aqua-planet without land and a 50 m deep slab ocean. The slab ocean is inert, so it stores heat locally but it does not redistribute heat horizontally. Previous studies indicated that ocean dynamics can have a significant impact on habitable planets, especially those near the outer edge of the habitable zone (Hu & Yang 2014; Del Genio et al. 2019; Yang et al. 2019). However, here we focus on planets near the inner edge of the habitable zone. For such planets the planetary heat transport from day to nightside is dominated by the atmosphere (Yang et al. 2019) and slab ocean simulations are sufficiently accurate to estimate important global-mean quantities, such as the water vapor mixing ratio in the upper atmosphere (Fujii et al. 2017).

In this work, ExoCAM is configured similar to the simulations in Kopparapu et al. (2016), Komacek & Abbot (2019), and Zhang & Yang (2020). The initial condition is set to the ExoCAM default. The default spatial resolution is $4^\circ \times 5^\circ$ in latitude and longitude with 40 vertical levels from the surface up to 1 hPa. Based on sensitivity tests in which we changed the horizontal resolution (see Appendix A.2), the most rapidly rotating planets use a higher horizontal resolution of $1.9^\circ \times 2.5^\circ$; our model configurations are listed in Appendix B.1. The reference albedo of the ocean surface at a zenith angle of 60° is 0.06 in the visible and 0.07 in the near-infrared. The calculations use a time step of 30 minutes, with radiative transfer updated every two time steps. All simulations are run to statistical equilibrium, which we define as when the global-mean net top-of-atmosphere flux (absolute difference between incoming stellar and outgoing long-wave) averaged over one Earth year reaches 3 W m^{-2} or less. Typically, the GCM equilibrates within 35–45 Earth years. We analyze 10 Earth-year-averaged outputs after statistical equilibrium.

3. The Bat Rotation Regime

3.1. New Dynamical Regime at High Rotation

To explore the impact of rotation, we first fix the stellar spectrum and stellar constant in ExoCAM to that of a young white dwarf and only vary the planet's rotation rate. We consider rotation rates ranging from a slow 20 days, representative of a habitable planet around an early M dwarf, over a moderate 10 and 2 days, representative of a habitable planet around a late M dwarf, to a rapid 0.5 days, representative of a habitable planet around a white dwarf (sensitivity tests suggest that the model's horizontal resolution is sufficient to resolve the Rossby deformation radius even at such rapid rotation; see Appendix A.2). Figure 1 shows the resulting surface temperature and zonal mean zonal wind maps.

Our simulations at slow and moderate rotation match those discussed in previous studies of M dwarf planets (Noda et al. 2017; Haqq-Misra et al. 2018; Komacek & Abbot 2019; Cohen et al. 2024). Due to the close overlap between our results and those in Haqq-Misra et al. (2018) we use the same dynamical regime labels, namely slow rotator, Rhines rotator, and rapid

rotator. Figure 1 shows that as the rotation rate increases, the surface temperature changes from being dominated by a hemispherical day–night temperature gradient (slow rotator and Rhines rotator), toward a zonally banded structure (rapid rotator). In all cases, the hottest point on the surface is at the equator. Similarly, the atmospheric circulation changes from a global day–night overturning cell with weak equatorial superrotation (slow rotator), toward a zonally dominated circulation with increased equatorial superrotation and a pair of strong eastward midlatitude jets (Rhines rotator and rapid rotator).

Surprisingly, as the rotation increases further and exceeds one rotation per day, a new dynamical regime emerges (Figure 1, left column). The hottest surface temperatures move from the equator to the midlatitudes and take on the form of slanted zonal bands, while a cold tongue develops in the equatorial night hemisphere. Meanwhile, the zonal mean zonal winds also change dramatically. Equatorial superrotation largely disappears, except in a region of remnant weak superrotation below 500 hPa. Above 500 hPa at the equator, as well as throughout the entire atmospheric column off the equator, the zonal winds reverse sign and the atmosphere develops a strong westward, i.e., subrotating, jet. The fact that the hottest surface temperatures move off the equator and the zonal winds flip sign at the equator distinguishes this simulation from the dynamical regimes of M dwarf planets discussed in Haqq-Misra et al. (2018), but are consistent with the most rapidly rotating simulations ($P \lesssim 1$ day) presented in previous theoretical studies of tidally locked planets (Merlis & Schneider 2010; Noda et al. 2017; Komacek & Abbot 2019; Cohen et al. 2024).

Based on its distinctive surface temperature pattern we name the most rapidly rotating simulation a bat rotator, as illustrated in Figure 2. In the rest of this paper, we define bat rotators as planets with their hottest surface temperature located off the equator (Figure 2, right panel) and with net subrotating winds at the equator. In practice we evaluate these criteria based on whether the latitude of the maximum in the zonal mean surface temperature is more than one equatorial Rossby deformation radius away from the equator, and whether the (mass-weighted) vertical and zonal mean zonal wind within one Rossby deformation radius of the equator is westward

$$|y_{\max \bar{T}_s(\text{lat})}| > L_{Ro}, \quad (2a)$$

$$\bar{U}_{eq} < 0. \quad (2b)$$

Here $y_{\max \bar{T}_s(\text{lat})}$ is the distance between the latitude of the zonal mean surface temperature maximum and the equator, L_{Ro} is the equatorial Rossby deformation radius, and \bar{U}_{eq} is the vertical and zonal mean zonal wind near the equator. We evaluate L_{Ro} as $L_{Ro} = \left(\frac{a}{2\Omega} \right)^{\frac{1}{2}} \left(\frac{RgH}{c_p} \right)^{\frac{1}{4}}$, which assumes an isothermal atmosphere; a is the planet radius, Ω the planetary rotation rate, R the specific gas constant, g is the surface gravity, H is the scale height, and c_p is the specific heat of air at constant pressure.

3.2. Features of the Bat Rotation Regime

The emergence of a new dynamical regime at rapid rotation has broad implications for climates on white dwarf planets. Figure 3 shows additional output variables from the idealized simulations in Figure 1. To highlight the dominant impact of rotation, we do not include the Rhines rotator and only compare the bat rotator against rapid and slow rotators.

Figure 3(b) shows maps of surface pressure together with arrows indicating near-surface horizontal winds. On the slow

⁴ ExoCAM source code: <https://github.com/storyofthewolf/ExoCAM>.

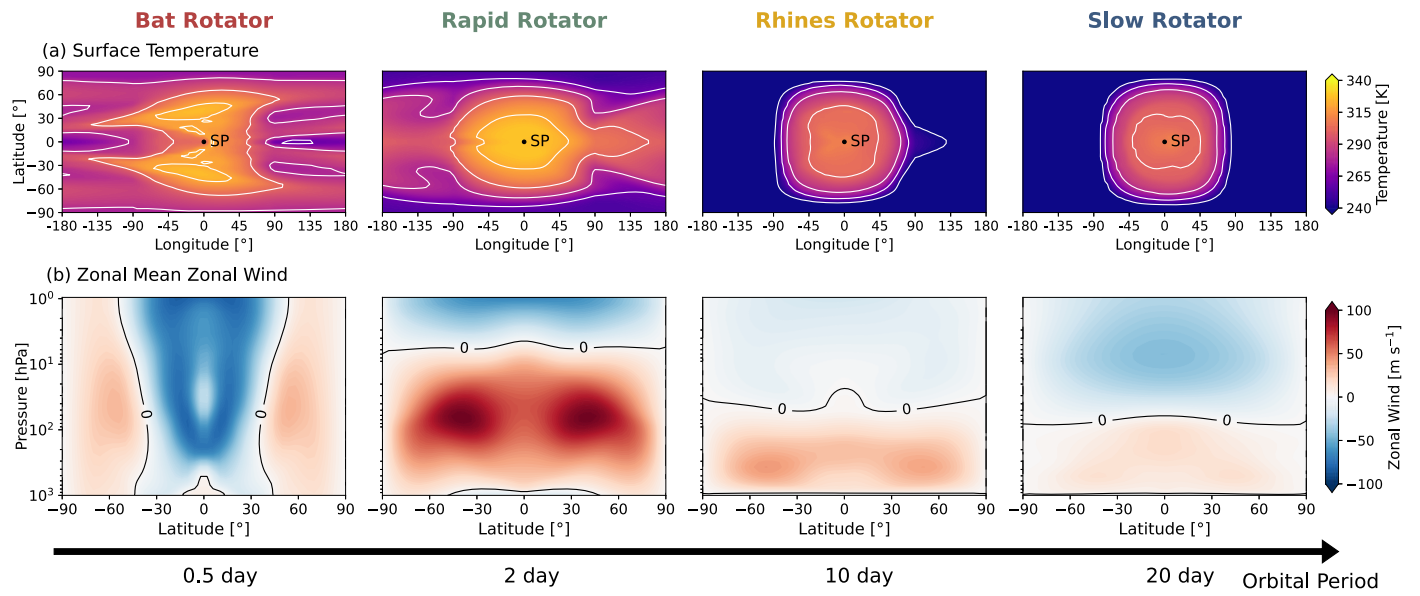


Figure 1. (a) Surface temperature and (b) zonal mean zonal wind as a function of rotation period. From left to right: bat rotator ($P = 0.5$ days; this work), compared to a rapid rotator ($P = 2$ days), Rhines rotator ($P = 10$ days), and slow rotator ($P = 20$ days). Dynamical regimes for the slower rotating planets are defined as in Haqq-Misra et al. (2018). In (a), “SP” corresponds to the substellar point. In (b), red vs. blue shading represent eastward vs. westward winds. The simulations assume a 10,000 K white dwarf and 2.12 times Earth’s instellation.

rotator, the surface pressure and surface temperature coincide closely. In line with a day–night thermally direct circulation, surface horizontal winds converge at the substellar point (SP) where the surface pressure is lowest. On the rapid rotator a high-pressure center forms on the nightside midlatitudes, indicative of a stationary Rossby wave with a zonal wavenumber of one. Near-surface winds no longer directly point from high to low pressure, suggesting horizontal gradients are balanced by both friction and Coriolis forces (frictional–geostrophic balance). On the bat rotator, the surface pressure differences are larger and the midlatitude winds are more closely aligned with the pressure contours than on the rapid rotator, consistent with a flow dominated by purely geostrophic balance.

The surface pressure map of the bat rotator is consistent with its distinctively banded surface temperature pattern (compare Figures 3(a) and (b)). The high-pressure centers in the midlatitudes are flanked by low-pressure centers at the poles. The resulting geostrophic flow around these centers transports sensible and latent heat to the nightside, which helps support the banded, bat-like, surface temperature pattern. Similarly, the pressure centers at low latitudes are twisted and banded, with a high-pressure band on the nightside equator. Air sinks in this region and the horizontal winds are weak, suggesting less exchange with heat from the dayside, which helps to sustain the cold tongue at the equator.

Figure 3(c) shows maps of cloud fraction. Previous work found that more rapid rotation on M dwarf planets weakens the convergence of zonal winds near the SP and decreases dayside cloud cover (Kopparapu et al. 2016; Haqq-Misra et al. 2018; Komacek & Abbot 2019). Surprisingly, we find that the bat rotator is cloudier than the rapid rotator inside the substellar region (defined as within 30° of the SP; see Figure 3(c)). Consequently, the substellar region on a bat rotator receives less shortwave radiation, promoting cooler surface temperatures at the equator. In addition, there are banded cloud-free regions in the bat wings on the dayside between 30° and 60° . These regions receive more shortwave radiation, consistent with the bat wings also containing the hottest surface temperatures (compare Figures 3(a) and (c)).

Finally, consistent with equatorial superrotation on the rapid rotator versus subrotation on the bat rotator, the clouds near the SP are shifted east on the rapid rotator versus west on the rapid rotator (Figure 3(b)).

Figure 3(d) displays the zonal mean winds. The rapid rotator is dominated by two tropospheric eastward jets that peak in the midlatitudes (30° – 60°), and has superrotation at the equator. In contrast, the bat rotator is dominated by a double-peaked westward jet, with subrotation equator-ward of 45° . Only near the surface, below 500 hPa, does the bat rotator still show weak equatorial superrotation. At high latitudes (45° – 90°), the bat rotator also has two eastward jets, but the jets are moved poleward and are weaker than on the rapid rotator.

Overall, the dynamics of the bat rotation regime are thus quite distinct from the dynamics reported in most previous studies of tidally locked planets. In agreement with Rhines scale arguments, which predict that jet width decreases with increasing rotation (e.g., Showman & Kaspi 2013), the bat rotator features more zonal jets than the rapid rotator. However, previous studies found that more rapid rotation strengthens equatorial superrotation (Merlis & Schneider 2010; Kopparapu et al. 2016; Haqq-Misra et al. 2018), whereas here equatorial superrotation disappears almost entirely and is replaced by strong subrotation. The emergence of subrotation is consistent with thermal wind balance. On a bat rotator the midlatitudes are hotter than the equator, so any geostrophically balanced low-latitude jet should flip from eastward to westward (note this argument does not hold directly at the equator where the Coriolis force is zero, consistent with the fact that the subrotating jet on the bat rotator is strongest off the equator; see Figure 3(d)). Finally, the equator-to-pole temperature contrast on the bat rotator is also lower than on the rapid rotator (see Figure 3). This decreasing trend is opposite to that found in previous studies of both tidally locked and non-tidally locked planets (Kaspi & Showman 2015; Haqq-Misra et al. 2018), which showed that higher rotation leads to smaller eddies and less efficient pole-ward energy transport.

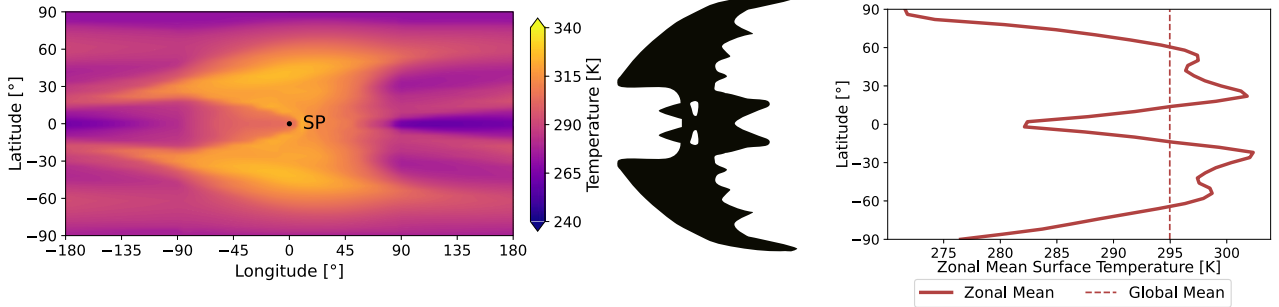


Figure 2. The surface temperature map and zonal mean surface temperature profile of a typical bat rotator. We name the bat rotation regime after the shape of its surface temperature map. Left: “SP” shows the substellar point. The simulation shown is identical to Figure 1, left column.

3.3. Distribution of Bat Rotators around White Dwarfs

How significant is the bat rotation regime for white dwarf planets? To address this question, we explored different combinations of instellation and stellar effective temperature with the GCM. The assumed host stars range from hot young white dwarfs (10,000 K) to cool old white dwarfs (3500 K). Planetary rotation rate is varied self-consistently, with orbital periods ranging from 3.4 days (coldest simulation orbiting a 10,000 K white dwarf) down to 0.13 day (hottest simulation orbiting a 3500 K white dwarf); see Appendix Table 1.

Figure 4 shows the resulting simulations as a function of rotation rate. The rotation rate is also expressed using the nondimensional Rossby deformation radius, defined as the equatorial Rossby deformation radius L_{Ro} divided by the planetary radius a . In all cases the equatorial Rossby deformation radius is smaller than the planetary radius, $L_{Ro}/a < 1$, which means equatorial waves cannot propagate globally due to the influence of rotation (Leconte et al. 2013; Koll & Abbot 2015). To categorize the simulations, we classify a simulation as a bat rotator if it satisfies Equations (2b); all other simulations are classified as rapid rotators.

We find little to no overlap between bat rotators and rapid rotators, supporting our classification of them as distinct dynamical regimes (also see Noda et al. 2017). Figure 4(a) shows the equatorial zonal and vertical mean zonal wind \bar{U}_{eq} , defined above. All simulations either display strong equatorial superrotation or weak to strong subrotation; notably, we find no simulations with intermediate weak superrotation. Similarly, Figure 4(b) shows that the zonal mean surface temperature maximum in all simulations is either located close to the equator, or significantly off the equator ($y_{max, Ts}/L_{Ro} = 1.5$ at $P = 0.5$ days translates to about 26°), with no intermediate values. Finally, bat rotators tend to be hotter than rapid rotators (see Figure 4(c)). This is because instellation and orbital period are varied self-consistently, so planets that receive more stellar flux tend to be closer to their host stars and rotate more rapidly. Therefore, the bat rotation regime is most relevant for the inner edge of the habitable zone around white dwarfs.

3.4. Predicting the Onset of Bat Rotation

Figures 3 and 4 show that the transition from rapid rotators to bat rotators is abrupt and occurs at a critical rotation period of about 1 day. Can this critical rotation period be understood using theory? Similarly, why do our rocky planet simulations at $P \sim 1$ day develop equatorial subrotation and midlatitude temperature maxima, whereas hot Jupiters at $P \sim 1$ day have equatorial superrotation and equatorial hot spots (Showman & Polvani 2011)?

In this section we offer a tentative explanation based on shallow water theory.

Briefly, previous work developed analytic solutions to the shallow water equations on the equatorial beta plane (Gill 1980; Wu et al. 2001; Showman & Polvani 2011). Below we use the linear solutions from Showman & Polvani (2011), which consider the response of an atmospheric layer to heating and cooling, parameterized as Newtonian relaxation of the layer’s thickness over the radiative timescale τ_{rad} . Friction is included as Rayleigh drag with timescale τ_{drag} , representing friction from the planetary surface, vertical turbulent mixing, or momentum transport by breaking gravity waves. The shallow water equations are nondimensionalized by the equatorial Rossby deformation radius ($L = \sqrt{\frac{\sqrt{gH}}{\beta}}$), the gravity wave phase speed ($U_{wave} = \sqrt{gH}$), and the time for gravity waves to cross the deformation radius ($T = \sqrt{\frac{1}{\sqrt{gH}\beta}}$). The linearized and nondimensionalized equations read

$$\frac{\partial \eta}{\partial x} - yv = -\frac{u}{\hat{\tau}_{drag}}, \quad (3a)$$

$$\frac{\partial \eta}{\partial y} + yu = -\frac{v}{\hat{\tau}_{drag}}, \quad (3b)$$

$$\frac{\partial u}{\partial x} + \frac{\partial v}{\partial y} = S(x, y) - \frac{\eta}{\hat{\tau}_{rad}}. \quad (3c)$$

Here x and y are eastward and northward distances, respectively, u and v are the eastward and northward horizontal velocities, respectively, $\hat{\tau}_{drag}$ and $\hat{\tau}_{rad}$ are dimensionless timescales, i.e., $\hat{\tau} = \frac{\tau}{T}$, and η is the deviation of the atmospheric layer’s thickness from its reference thickness H . Note that if all other parameters are held fixed, increasing the planet’s rotation (larger β) decreases L and T , which increases $\hat{\tau}_{drag}$ and $\hat{\tau}_{rad}$.

For finite τ_{drag} , solutions to these equations take on the meridional structure of the parabolic cylinder functions $\psi_n(y)$ (Wu et al. 2001; Showman & Polvani 2011)

$$\psi_n(y) = \exp \left[-\frac{1}{2} \left(\frac{y}{\mathcal{P}} \right)^2 \right] H_n \left(\frac{y}{\mathcal{P}} \right), \quad (4)$$

which are Gaussians times Hermite polynomials H_n ; the first few Hermite polynomials are $H_0(x) = 1$, $H_1(x) = 2x$, and $H_2(x) = 4x^2 - 2$, and the Hermite polynomials are related via $H_{n+1}(x) = 2xH_n(x) - H'_n(x)$. Here $\mathcal{P} = \left(\frac{\tau_{rad}}{\tau_{drag}} \right)^{\frac{1}{4}}$ is the fourth root of the Prandtl number. For tidally locked planets, if the

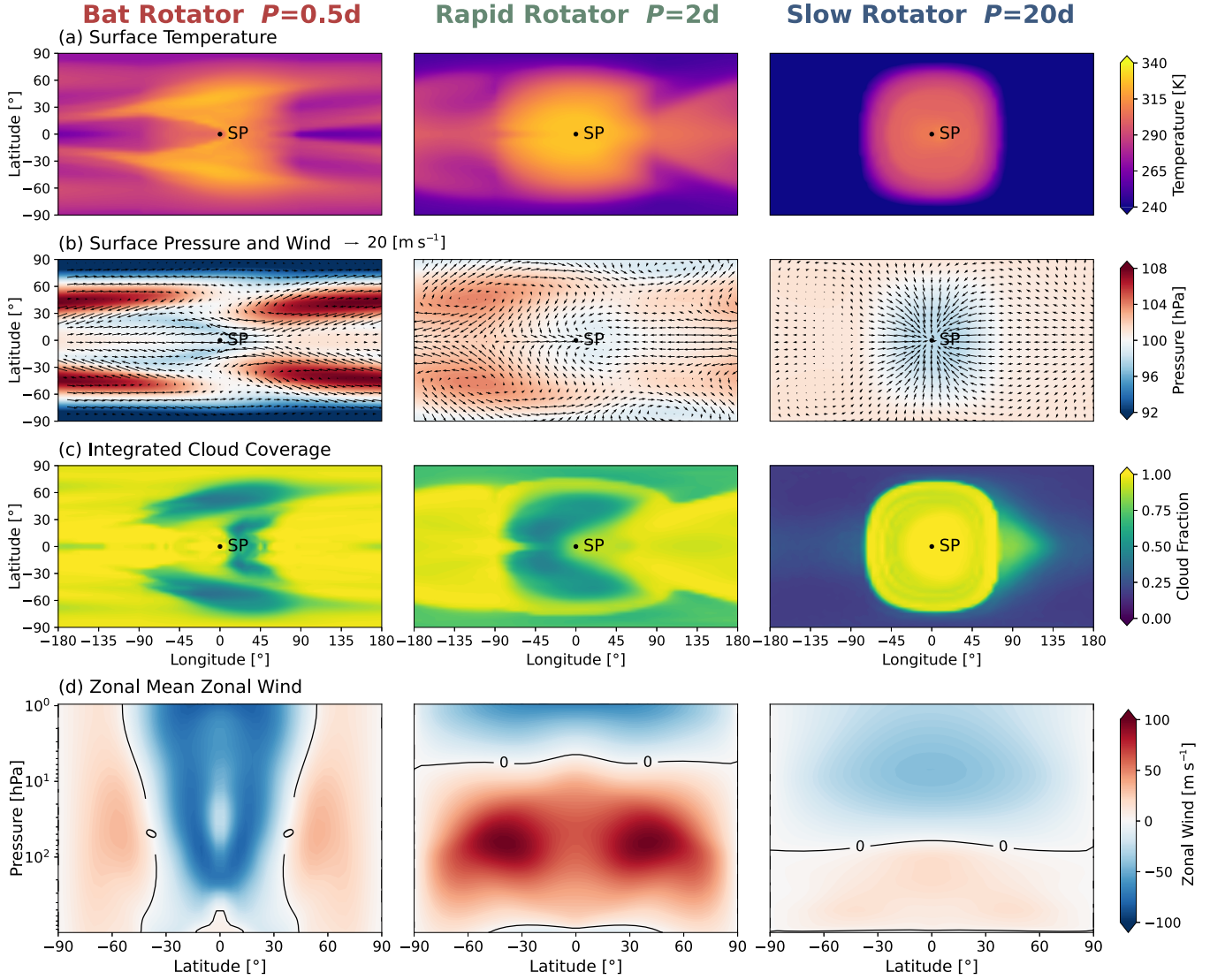


Figure 3. Climate comparison of a bat rotator, a rapid rotator, and a slow rotator. “SP” corresponds to the substellar point in each map. The three rotators are orbiting a 10,000 K white dwarf and receiving 2.12 times Earth’s insulation. Except for the orbital periods set at 0.5, 1.96, and 20 days, respectively, the simulations are configured identically. From top to bottom, the panels are, respectively, maps of surface temperature, surface pressure, with surface wind at 970 hPa, total cloud fraction, and zonal mean zonal wind.

thermal forcing and solutions vary sinusoidally in longitude with dimensionless zonal wavenumber k , the pattern of the thermal forcing can be represented as

$$S(x, y) = \sum_{n=0}^{\infty} S_n e^{ikx} \psi_n(y), \quad (5)$$

while the layer’s thickness (proportional to the atmosphere’s temperature) is represented as

$$\eta(x, y) = \sum_{n=0}^{\infty} \hat{\eta}_n(y, \hat{\tau}_{\text{rad}}, \hat{\tau}_{\text{drag}}) e^{-\frac{1}{2}(\frac{y}{P})^2} e^{ikx}, \quad (6)$$

where $\hat{\eta}_n(\frac{y}{P})$ are complex functions of $\frac{y}{P}$. Equation (6) shows that $\eta(x, y)$ is determined by only two nondimensional parameters, $\hat{\tau}_{\text{rad}}$ and $\hat{\tau}_{\text{drag}}$. These are equivalent to 3D parameters, τ_{rad} , τ_{drag} , and T , which represent radiative damping, frictional damping, and geostrophic adjustment, respectively.

To investigate the transition between rapid rotators and bat rotators, we evaluate solutions of $\eta(x, y)$ for different $\hat{\tau}_{\text{rad}}$ and $\hat{\tau}_{\text{drag}}$ following the methods in Showman & Polvani (2011). Figure 5(a) shows that, when the dimensionless timescales are short (at slow rotation, $\hat{\tau}_{\text{rad}} \hat{\tau}_{\text{drag}} \sim \mathcal{O}(1)$), the maximum and minimum thermal (height) perturbations η lie at the equator and are close to the substellar and antistellar points. As the timescales get longer (at rapid rotation, $\hat{\tau}_{\text{rad}} \hat{\tau}_{\text{drag}} \sim \mathcal{O}(100)$), the height extrema shift westward and off the equator while cyclonic and anticyclonic gyres develop around them. In the shallow water solutions, the shift between on-equator and off-equator maxima is gradual instead of abrupt because the solutions are linearized and exclude nonlinear feedback. Nevertheless, Figure 5(a) shows the linearized shallow water solutions transition from a large day–night gradient to a more banded structure with an off-equator height maximum, crudely matching the transition from slow over rapid to bat rotators in our GCM simulations (see Figure 1).

What combination of $\hat{\tau}_{\text{rad}}$ and $\hat{\tau}_{\text{drag}}$ is necessary to produce bat-like behavior with off-equator hot spots in the shallow

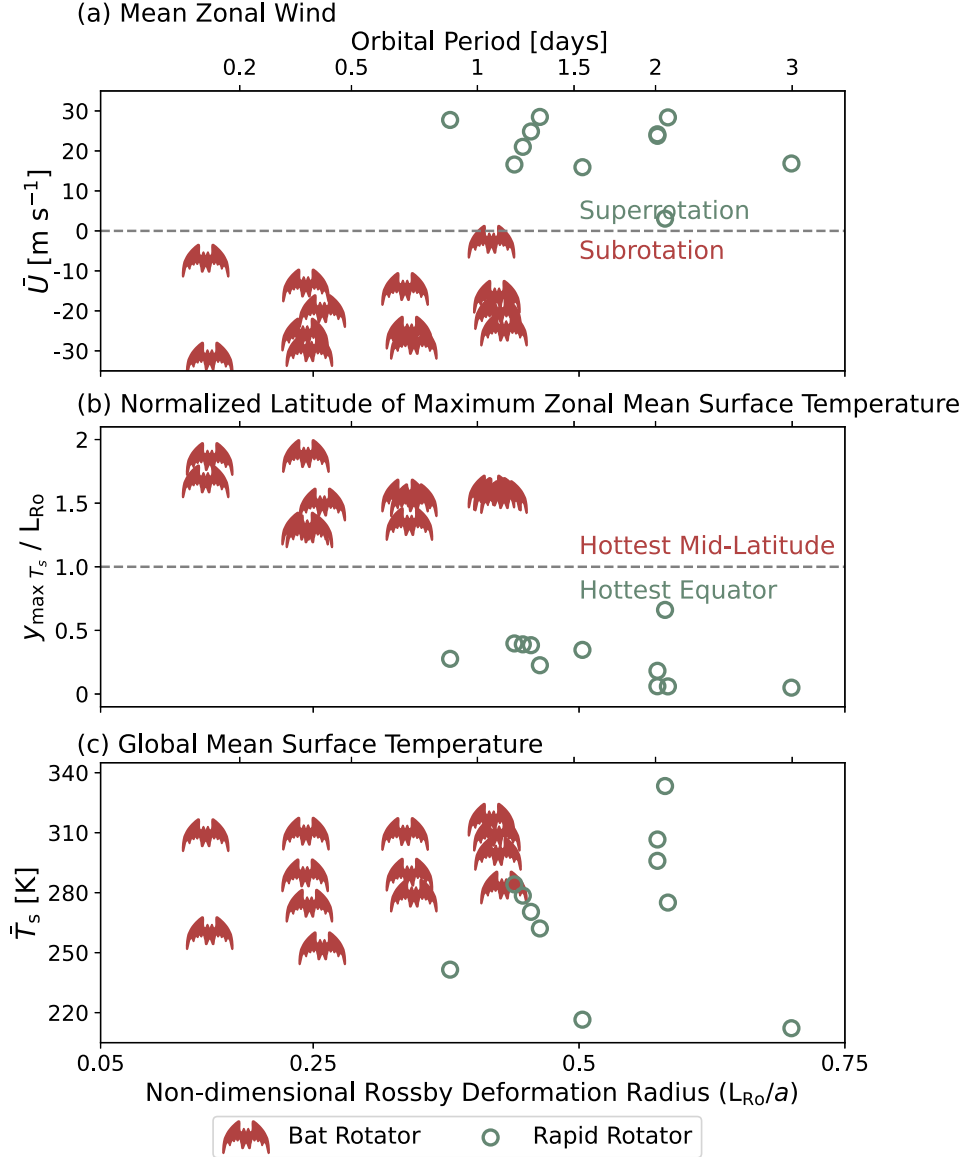


Figure 4. Distribution of bat rotators and rapid rotators in our simulations as a function of orbital period and nondimensional Rossby deformation radius. (a) Zonal and vertical mean zonal wind near the equator (within one Rossby deformation radius from the equator). The vertical mean is computed using a mass-weighted average. (b) Distance between the equator and zonal mean surface temperature maximum, normalized by the equatorial Rossby deformation radius. (c) Global-mean surface temperature. Red bat patterns and green circles represent bat rotators and rapid rotators, respectively.

water equations? Figure 5(a) suggests a threshold of $\hat{\tau}_{\text{rad}} \hat{\tau}_{\text{drag}} \sim \mathcal{O}(10)$. To quantify this threshold, we numerically analyzed the analytical solutions from Showman & Polvani (2011) to find the latitude \tilde{y} at which the height field η reaches its maximum. Figure 5(c) shows \tilde{y} as a function of $\hat{\tau}_{\text{rad}}$ and $\hat{\tau}_{\text{drag}}$. The plot shows $\tilde{y}(\hat{\tau}_{\text{rad}}, \hat{\tau}_{\text{drag}})$ is approximately symmetric about the diagonal, so it only depends on the product $\hat{\tau}_{\text{rad}} \hat{\tau}_{\text{drag}}$. We take $\tilde{y} = 1$ as the critical value which distinguishes between solutions with on-equator versus off-equator height maxima (black line in Figure 5(c)). This boundary can be fitted as $\hat{\tau}_{\text{rad}} \hat{\tau}_{\text{drag}} \approx 13$. Converting the boundary to dimensional quantities, the shallow water equations therefore transition toward bat-like solutions at a threshold orbital period of

$$P_{\text{bat}} \approx \tau_{\text{rad}} \tau_{\text{drag}} \frac{U_{\text{wave}}}{a}. \quad (7)$$

Note, no numerical factors remain a in the equation because $\hat{\tau}_{\text{rad}} \hat{\tau}_{\text{drag}} \approx 13$ is canceled almost exactly by the factor of 4π which arises when converting from β to P .

Next, we evaluate the value of $\tau_{\text{rad}} \tau_{\text{drag}} \frac{U_{\text{wave}}}{a}$ for our GCM simulations. To do so we assume an internal gravity wave with phase speed $U_{\text{wave}} \sim 20 m s^{-1}$, consistent with typical gravity wave speeds in Earth's tropics (Kiladis et al. 2009; Vallis 2017). The radiative timescale is equal to $\tau_{\text{rad}} = \frac{c_p p}{4\sigma T_e^3 g}$, where $c_p \approx 1004.64 J (kg K)^{-1}$ is the isobaric specific heat of air, p is the surface pressure, σ is the Stefan–Boltzmann constant, T_e is the effective radiating temperature, and g is the surface gravity. To evaluate τ_{rad} we use T_e derived from the GCM's global-mean outgoing long-wave radiation; we find τ_{rad} is about 25–30 days (2.5×10^6 s). Assuming drag in the GCM is mostly from surface friction, $\tau_{\text{drag}} = \frac{U_{\text{ph}}}{f}$, where U is the horizontal wind at 970 hPa, ρ is the air density at 970 hPa, h is the thickness of the planetary boundary layer, and f is the zonal surface stress. Evaluating these parameters using the GCM output, we find a drag timescale of about 5×10^4 s, or less than 1 day. For comparison, typical radiative and drag timescales for

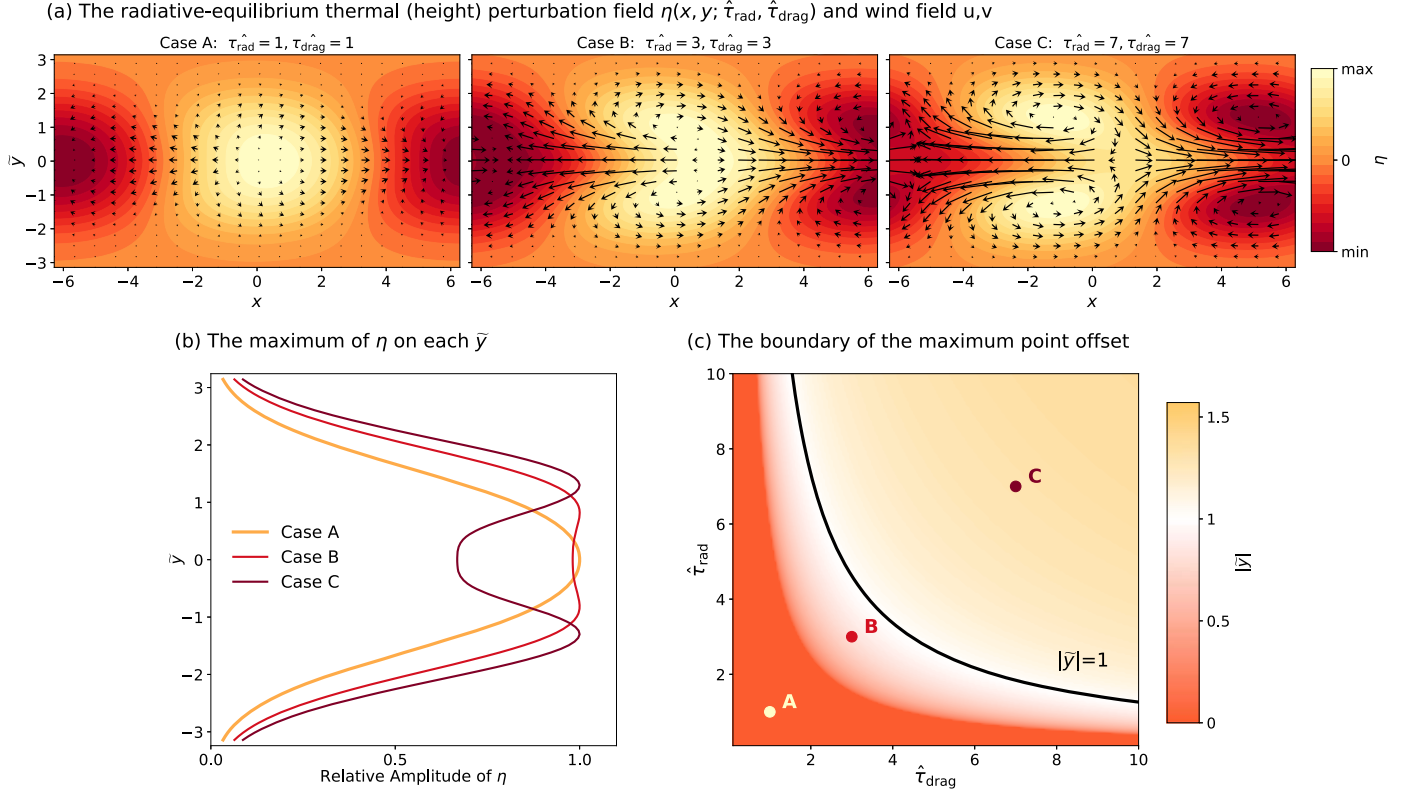


Figure 5. The shallow water equations qualitatively reproduce the transition from rapid to bat rotator. (a) Analytic solutions of the linearized shallow water equations (Equations (3a)–(3c)) for dimensionless zonal wavenumber $k = 0.5$. Colors represent the height perturbation field and arrows represent horizontal winds. Assuming all other parameters are held fixed, rotation increases from Case A to C. (b) The maximum of η at each nondimensional latitude \bar{y} . The value of η at each latitude is normalized by the global maximum of η . (c) Absolute value of the latitude at which η is largest, $|\bar{y}|$, as a function of the dimensionless timescales $\hat{\tau}_{\text{rad}}$ and $\hat{\tau}_{\text{drag}}$. Black line shows $|\bar{y}| = 1$. Dark colors correspond to the height maximum at the equator and light colors correspond to the height maximum at midlatitudes.

Earth are 30 days and 5–10 days (Vallis 2017), respectively, and idealized GCM simulations often use a drag timescale of 1 day (Held & Suarez 1994; Penn & Vallis 2018).

Plugging these values into Equation (7), the threshold toward bat-like rotation predicted by the linearized shallow water equations is

$$P_{\text{bat}} \approx 4 \text{ days.} \quad (8)$$

This prediction is larger than the threshold $P \sim 1$ days we numerically found in the GCM by a factor of 4; that is, both values agree to within an order of magnitude. To explain the remaining mismatch between theory and the GCM, note that the GCM includes additional mechanisms which are missing from the linearized shallow water equations. In the GCM the transition from rapid rotation to bat rotation is abrupt (see Figure 4), and thus is likely related to nonlinear dynamical terms. Similarly, the GCM includes feedbacks from condensation and clouds, and the solutions from Showman & Polvani (2011) restrict the shallow water equations to an equatorial beta plane, whereas the GCM incorporates full spherical geometry. Any of these factors could create a mismatch by a factor of a few. We therefore consider the shallow water equations to be in qualitative agreement with our far more sophisticated GCM simulations.

As a sanity check, we also analyzed the predicted transition between day–night-dominated solutions to solutions with eastward hot spot offsets in the shallow water equations (Case A versus B in Figure 5(a)). The transition toward eastward hot spot offsets occurs at $\hat{\tau}_{\text{rad}} \hat{\tau}_{\text{drag}} \sim \mathcal{O}(1)$, or 1 order of magnitude slower rotation than the transition to bat-like behavior. This qualitatively

matches the transition between slow and rapid rotators in the GCM, which occurs at an orbital period of $P \sim 20$ days.

What does our result tell us about dynamical regimes on rocky planets versus hot Jupiters? We use Equation (7) to scale from $P \sim 1$ day for rocky planets to gas giants. Largely by virtue of being hot, the radiative timescale on hot Jupiters is shorter than on Earth-like planets. Using representative hot Jupiter values ($T_{\text{eq}} \sim 1500$ K, $p \sim 1$ bar, $g \sim 20 \text{ m s}^{-2}$, c_p corresponding to H₂), $\tau_{\text{rad}} \approx 1$ day. Drag timescales for hot Jupiters are widely uncertain, ranging from $\mathcal{O}(10^8)$ s for magnetic drag (Perna et al. 2010), down to $\mathcal{O}(10^5)$ s for frictional dissipation associated with shear instabilities (Koll & Komacek 2018); here we assume $\tau_{\text{drag}} \approx 1$ day. Finally, we assume a wave speed smaller than the speed of sound by about a factor of 2, $U_{\text{wave}} \sim 10^3 \text{ m s}^{-1}$, and a radius equal to that of Jupiter. Using these values and $P \sim 1$ day for rocky planets, we find hot Jupiters should transition toward bat-like rotation at an orbital period of $P \sim 0.3$ days (equivalently, at an orbital distance less than 0.01 au). Such high rotation rates and small orbits are generally not accessible to hot Jupiters, as gas giants are rare on ultrashort orbits around main-sequence stars (Winn et al. 2018). The bat rotation regime might thus only be accessible to rocky planets.

4. Inner Edge of Habitable Zone Shaped by Bat Rotation Regime

Up to now our results show that habitable white dwarf planets on ultrashort orbits exhibit novel atmospheric dynamics. How do these dynamics influence the habitable zone around white dwarfs?

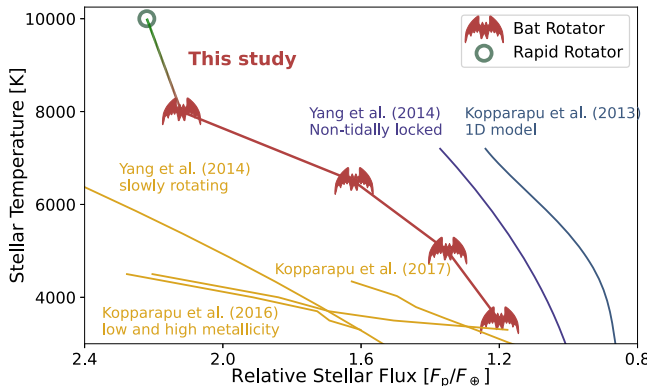


Figure 6. The RGHL around white dwarfs, and comparison to previous studies. The x -axis shows the maximum stellar flux at the inner edge of the habitable zone relative to Earth’s solar constant, and the y -axis shows the stellar effective temperature. The red-green line shows the estimated RGHL for white dwarfs, where bat and circle symbols represent bat rotators and rapid rotators (same as in Figure 4), respectively. Other colored lines show previous work: RGHL for slowly rotating tidally and locked planets orbiting M dwarfs (yellow; Yang et al. 2013; Kopparapu et al. 2016, 2017), RGHL for rapidly rotating and non-tidally locked planets (purple; Yang et al. 2014), and RGHL based on 1D calculations (blue; Kopparapu et al. 2013).

4.1. Runaway Greenhouse Limit

To investigate the inner edge of the habitable zone, we adopt a methodology similar to that of Kopparapu et al. (2016). We move planets closer to the star by simultaneously increasing the stellar flux and rotation rate until the simulations become unstable. The last converged simulation is taken as a proxy for the RGHL (for the full list of converged and nonconverged simulations see Appendix Figure 14).

Figure 6 shows the estimated RGHL as a function of stellar effective temperature. In line with previous habitability studies (e.g., Kopparapu et al. 2013; Yang et al. 2014; Kopparapu et al. 2017; Haqq-Misra et al. 2018), the RGHL for white dwarfs moves closer to the star at higher stellar temperature. This is because hotter stars give off bluer radiation, which increases the planetary albedo via stronger Rayleigh scattering and weaker atmospheric absorption in the near-infrared (e.g., Kopparapu et al. 2016). In addition, the RGHL for white dwarfs is intermediate between two limits studied in previous work; it is closer to the star than the RGHL for non-tidally locked planets (red-green versus purple line), but it is further away than the RGHL for tidally locked planets around M dwarfs (red-green versus yellow lines). Note that for most white dwarfs the hottest converged simulation is a bat rotator; only for a 10,000 K white dwarf is the hottest converged simulation a rapid rotator (bat versus circle symbols in Figure 6).

Why does the RGHL for white dwarfs lie in between that for rapidly rotating non-tidally locked planets and that for slowly rotating tidally locked planets? On the one hand, being tidally locked promotes higher dayside cloud cover, which increases planetary albedo (Yang et al. 2013). On the other hand, once a planet is tidally locked, a shorter orbital period tends to reduce the dayside cloud cover, which reduces the planetary albedo (Yang et al. 2014; Kopparapu et al. 2016). White dwarf planets are both tidally locked and rotate more rapidly than M dwarf planets, matching the sequence in Figure 6. Our results are thus consistent with previous work on clouds and exoplanet habitability.

Next, we find that the onset of bat rotation helps extend the habitable zone. Figure 6 shows the white dwarf RGHL

generally moves inward for hotter stars, but the trend shows a distinct break at 10,000 K. This point corresponds to a shift from the hottest converged simulation being a bat rotator to being a rapid rotator (see symbols in Figure 6), suggesting that the onset of bat rotation triggers a stabilizing cloud feedback.

To investigate this cloud feedback in detail, we performed another set of idealized simulations for a 10,000 K host star in which we vary the rotation rate while keeping the instellation fixed. Varying the rotation from 5 days down to 0.5 days, we find the same trend as in prior studies; more rapid rotation tends to reduce the dayside cloud cover and planetary albedo (Yang et al. 2014; Kopparapu et al. 2016). However, Figure 7 shows that the general trend is interrupted by an abrupt jump at about 1.2 days, when the atmospheric circulation regime changes from rapid rotation to bat rotation. The global-mean surface temperature abruptly cools by ~ 30 K, while the planetary albedo increases by $\sim 10\%$ (Figures 7(a) and (b)). The increase in albedo is linked to a jump in high cloud fraction and cloud water path inside the substellar region. Both increase at 1.2 days, before decreasing again at even higher rotation (Figures 7(c) and (d)). Therefore, white dwarf planets exhibit the same general cloud feedback as M dwarf planets, in which higher rotation reduces cloud reflection and tends to shrink the habitable zone, but the shift from rapid rotation to bat rotation (not accessible to most habitable M dwarf planets) triggers a one-time increase in cloud reflection, expanding the habitable zone.

To estimate how clouds affect the overall width of the white dwarf habitable zone, we combined our GCM simulations for the inner edge of the habitable zone with prior 1D model results for the outer edge of the habitable zone (see Equation (9) below, from Kopparapu et al. 2013). Over the range of stellar temperatures for which Equation (9) is valid, we find that our GCM calculations increase the width of the habitable zone in instellation space by 50%–60% compared to estimates based on 1D models (Agol 2011; Kopparapu et al. 2013).

4.2. Moist Greenhouse Limit

Next, we investigate whether the habitable zone around white dwarfs is sensitive to gradual water loss via partial atmospheric escape to space, the so-called moist greenhouse. Habitable planets constantly lose water because H_2O in the upper atmosphere photodissociates into H and O. The lighter H preferentially escapes to space, gradually drying out the planet. A planet exceeds the moist greenhouse limit (MGHL) if it loses an Earth ocean’s worth of water within 4.5 Gyr; this occurs when the volume mixing ratio of stratospheric water vapor is higher than about 3×10^{-3} (Kasting et al. 1993). In practice, we evaluate this criterion using the global-mean specific humidity at the top of the model. One can also define the MGHL in terms of the top-of-model specific humidity in the substellar region only (Kopparapu et al. 2016); both MGHL definitions are consistent to within 1 order of magnitude so here we use the global-mean definition.

The top-of-model specific humidities of the last converged (i.e., hottest) simulations are shown in Figure 8. Unexpectedly, white dwarf planets with a host star cooler than 10,000 K never exceed the MGHL. This is because bat rotators have extremely dry upper atmospheres. Instead, the hot main-sequence planets considered in previous work featured stratospheric specific humidities ranging from 10^{-1} to $10^{-4} \text{ kg kg}^{-1}$ (Kopparapu et al. 2013, 2016; Wolf et al. 2017; Kopparapu et al. 2017), and thus typically exceeded the MGHL, where the hottest bat rotators have top-of-model

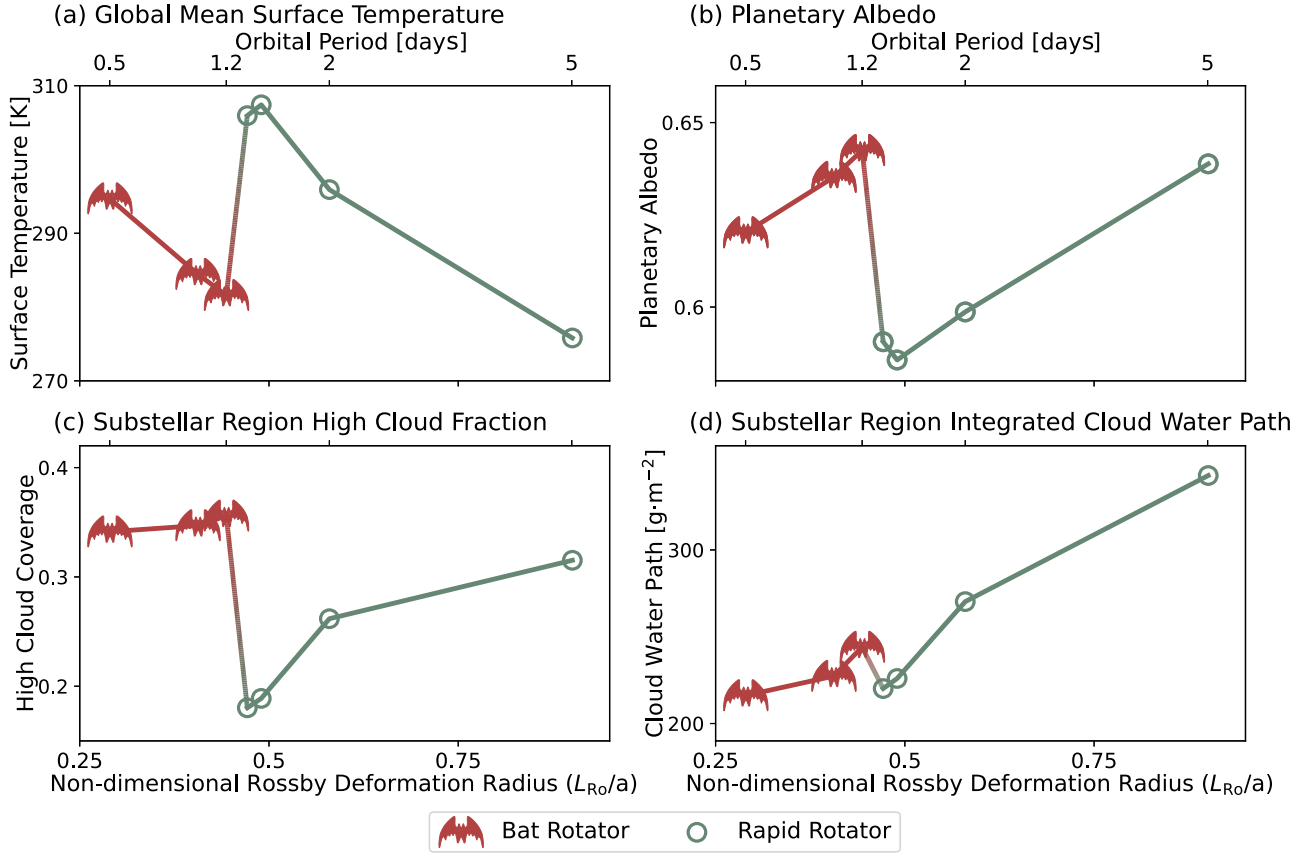


Figure 7. The transition to bat rotation is associated with an abrupt increase in cloud cover, which increases the planetary albedo. Simulations shown assume a fixed stellar spectrum and insolation (10,000 K, 2.12 times Earth’s insolation), and we only vary the rotation period. (a) Global-mean surface temperature. (b) Planetary albedo. (c) High cloud fraction in the substellar region (within 30° of the SP). (d) Integrated cloud water path in the substellar region. Bat and circle symbols represent bat rotators and rapid rotators (same as in Figure 4), respectively.

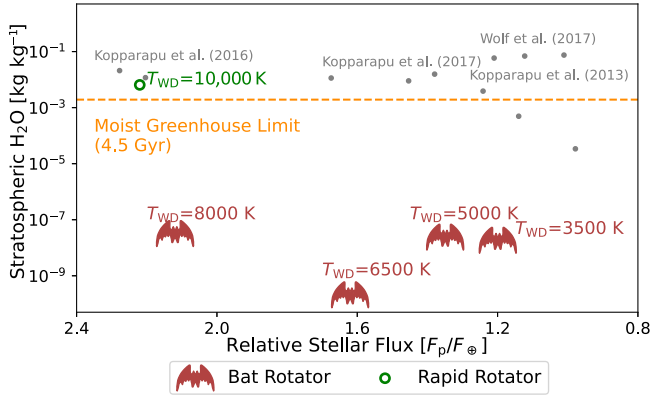


Figure 8. Bat rotators have exceptionally dry upper atmospheres, which suppresses the moist greenhouse. The x-axis shows the stellar flux of the last converged simulation and the y-axis shows the top-of-model specific humidity. The orange dashed line indicates a specific humidity of 1.93×10^{-3} kg kg $^{-1}$, corresponding to a volume mixing ratio of 3×10^{-3} . Gray dots show the results from previous studies for planets orbiting main-sequence stars (Kopparapu et al. 2013, 2016, 2017; Wolf et al. 2017), bat and circle symbols represent bat rotators and rapid rotators, same as in Figure 4, respectively, and T_{WD} is the effective temperature of the white dwarf.

specific humidities ranging from a dry 10^{-7} kg kg $^{-1}$ (drier than Earth’s stratosphere) down to an exceptionally dry 10^{-10} kg kg $^{-1}$.

The dry upper atmospheres of bat rotators are associated with a reversal in the dayside atmospheric circulation and the formation of anti-Hadley cells, which suppress the vertical transport of water

vapor. Figure 9 compares the dayside specific humidity, vertical water vapor transport, and meridional stream function for a bat rotator versus a rapid rotator; the shown simulations were chosen because they have almost identical global-mean surface temperatures and surface specific humidities. Despite the similar lower boundary, above 500 hPa the dayside mean specific humidity on the bat rotator is approximately 10 times less than on the rapid rotator, while the vertical water vapor transport is a factor of 2–10 less (Figures 9(a) and (b)).

To explain the difference in the vertical water vapor transport, Figure 9(c) displays the dayside zonal mean stream functions. On the rapid rotator the dayside circulation consists of air rising at the equator and sinking in the midlatitudes, akin to a Hadley cell. Surprisingly, on the bat rotator the circulation is flipped: above 600 hPa, air sinks at the equator and rises in the midlatitudes, forming an anti-Hadley cell (Charnay et al. 2015). The anti-Hadley cell is consistent with the unique surface temperature structure of the bat rotator. Its hottest temperatures are located in the midlatitudes, which reverses the meridional temperature gradient at low latitudes (Figures 2 and 3). Any thermally direct meridional (Hadley-like) circulation thus also has to reverse its direction. This helps to suppress deep convection at the equator and explains the ineffective vertical transport of moist air to the upper atmosphere. In addition, the stream function on the bat rotator is weaker than that of the rapid rotator, implying generally weaker vertical winds.

Overall, white dwarf planets are thus unlikely to experience a moist greenhouse; in contrast to most main-sequence planets, these

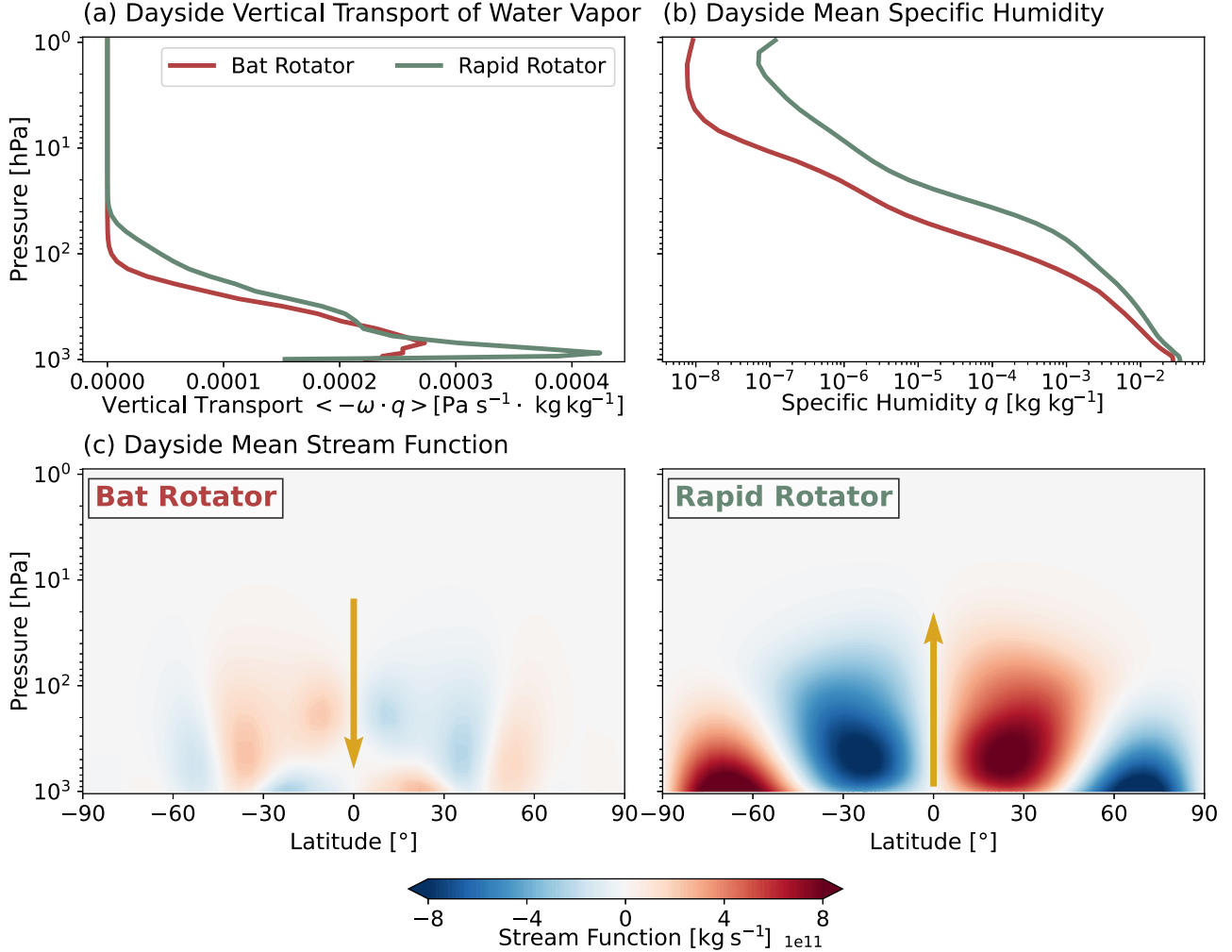


Figure 9. Bat rotators have drier upper atmospheres and less efficient vertical water transport than rapid rotators. (a) Dayside mean vertical transport of water vapor; a larger $< -\omega \cdot q >$ represents stronger upward transport of water vapor. (b) Vertical profile of the dayside mean specific humidity. (c) Zonal mean stream function on the dayside hemisphere; red shading (positive) indicates clockwise circulation and blue shading (negative) indicates counterclockwise circulation. Yellow arrows indicate the direction of vertical transport by the mean circulation at the equator. The bat rotator and the rapid rotator are orbiting a 10,000 K white dwarf and receiving 2.12 times Earth's insolation. The orbital period of the bat rotator and the rapid rotator are 0.5 days and 2 days, respectively, identical to those in Figure 3.

planets directly jump from a warm and temperate state into a runaway greenhouse (see Figure 8). Note, Kopparapu et al. (2016) also found that planets orbiting very low-mass M dwarfs can skip the moist greenhouse, because these stars emit redder radiation, which causes strong shortwave absorption and suppresses convection near the SP. In contrast, our results here hold over a wide range of stellar effective temperatures, highlighting the importance of planetary rotation for white dwarf planets.

5. Discussion

5.1. Significance of the Bat Rotation Regime

The bat rotation regime is important near the inner edge of the habitable zone around white dwarfs, but what about the rest of the habitable zone? In this section we argue most habitable planets around white dwarfs should also be bat rotators.

To assign different dynamical regimes to planets as a function of orbital period P we use criteria based on Haqq-Misra et al. (2018): planets with $P > 20$ days are assumed to be slow rotators, planets with $5 \text{ days} < P < 20$ days are Rhines rotators, planets with $1 \text{ day} < P < 5$ days are rapid rotators, and planets with $P < 1$ day are bat rotators. To

translate stellar effective temperature into stellar age, we use a model⁵ for white dwarfs with thin hydrogen envelopes adopted from Bédard et al. (2020). To estimate the outer edge of the habitable zone, we use a fit for the maximum greenhouse limit from 1D model calculations (Kopparapu et al. 2013),

$$S_{\text{eff}} = 0.3438 + 5.8942 \times 10^{-5} T_{\star} + 1.6558 \times 10^{-9} T_{\star}^2 - 3.0045 \times 10^{-12} T_{\star}^3 - 5.2983 \times 10^{-16} T_{\star}^4, \quad (9)$$

$$T_{\star} = T_{\text{WD}} - 5780, \quad 2600 \text{ K} \leqslant T_{\text{WD}} \leqslant 7200 \text{ K} \quad (10)$$

where S_{eff} and T_{WD} are the instellation at the outer edge of the habitable zone and the effective temperature of the white dwarf, respectively.

As white dwarfs age and cool, the habitable zone moves closer to the star; habitable planets around very old white dwarfs are thus in danger of tidal disruption. To estimate the tidal disruption boundary, we use an approximate solution of the Roche limit from Lissauer & de Pater (2019) valid for

⁵ https://github.com/SihaoCheng/WD_models

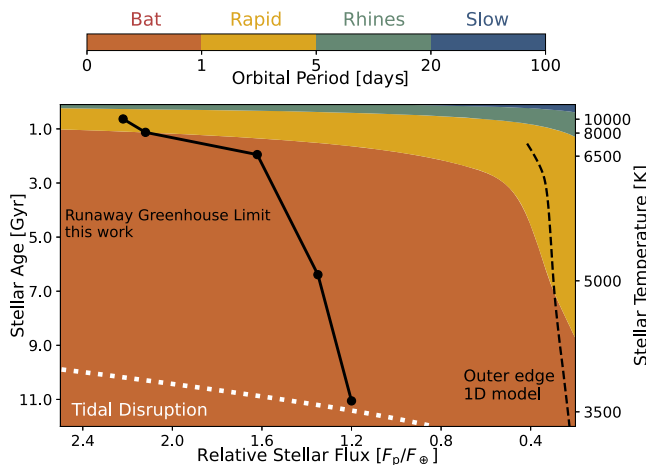


Figure 10. Estimated rotation regimes inside the habitable zone of white dwarfs with different stellar temperatures, as a function of the relative stellar flux. Colors denote different rotation regimes. The black solid line shows the inner edge of the habitable zone (RGHL, Section 4), the black dashed line shows the outer edge of the habitable zone (maximum greenhouse limit from Kopparapu et al. 2013), and the white dotted line shows the tidal disruption limit. The stellar mass of the white dwarf is fixed at $0.6 M_{\odot}$.

tidally locked liquid planets

$$d_{\text{tidal}} \approx 2.456 a_{\text{WD}} \left(\frac{\rho_{\text{WD}}}{\rho_p} \right)^{\frac{1}{3}}. \quad (11)$$

Here d_{tidal} is tidal disruption distance, a_{WD} and ρ_{WD} are the white dwarf radius and mean density, respectively, and ρ_p is the planet's mean density. Assuming a white dwarf with $M_{\text{WD}} = 0.6 M_{\odot}$ and a ρ_p equal to Earth's density, the tidal disruption distance for white dwarfs is $d_{\text{tidal}} = 0.0037$ au. The corresponding instellation S_{tidal} at this distance is

$$S_{\text{tidal}} = S_{\oplus} \left(\frac{T_{\text{WD}}}{T_{\odot}} \right)^4 \left(\frac{a_{\text{WD}}}{a_{\odot}} \right)^2 \left(\frac{1 \text{ au}}{d_{\text{tidal}}} \right)^2, \quad (12)$$

where S_{\oplus} is Earth's solar constant and a_{WD} and a_{\odot} are the radius of the white dwarf and Sun, respectively.

Figure 10 shows that most of the habitable zone around white dwarfs corresponds to the bat rotation regime. The only overlap with the rapid rotation regime occurs for white dwarfs younger than 3 Gyr. In addition, tidal disruption cuts off the habitable zone around stars older than about 11–12 Gyr. This upper limit for the oldest white dwarf systems that can still be habitable is about 50% more than the value estimated based on 1D models by Agol (2011), consistent with the fact that our white dwarf habitable zone based on 3D GCMs is wider than that based on 1D models (see Figure 6). Note that one could in principle sustain habitable conditions around white dwarfs even older than 12 Gyr, but doing so would require unconventional conditions that go beyond the conventional habitable zone (e.g., H₂-rich atmospheres; Pierrehumbert & Gaidos 2011).

5.2. Observation Implications

Can our theoretical predictions be tested? Previous work proposed using JWST transmission spectra to search for atmospheric absorption features and biosignatures on habitable white dwarf planets (Agol 2011; Kaltenegger et al. 2020). Here we consider a complementary proposal, namely using JWST

thermal observations to identify whether white dwarf planets have atmospheres in the first place (Selsis et al. 2011; Koll et al. 2019; Mansfield et al. 2019; Malik et al. 2019), and, with a larger investment of observing time, to empirically characterize the atmospheric dynamics regime of these planets.

Our calculation follows previous thermal phase curve calculations (Cowan & Agol 2008; Cowan et al. 2012; Koll & Abbot 2015; Koll 2022): we assume a white dwarf–planet system in a transiting geometry, with the planet's orbit viewed edge on. The planet emits thermal radiation isotropically. The intensity I at the top of the atmosphere is

$$I_{\text{TOA}}(\phi, \theta) = \frac{F_{\text{LW,TOA}}^{\uparrow}(\phi, \theta)}{\pi}, \quad (13)$$

where $F_{\text{LW,TOA}}^{\uparrow}$ is the GCM's flux of outgoing long-wave radiation, while ϕ and θ are the longitude and latitude on the planet, respectively. The planet's thermal flux received by a distant observer as a function of orbital phase ξ is (see Appendix C)

$$F(\xi) = \frac{\pi a^2}{d^2} \frac{\int_{-\frac{\pi}{2}}^{\frac{\pi}{2}} d\theta \int_{-\xi - \frac{\pi}{2}}^{-\xi + \frac{\pi}{2}} I_{\text{TOA}}(\phi, \theta) \cos(\phi + \xi) \cos^2 \theta d\phi}{\int_{-\frac{\pi}{2}}^{\frac{\pi}{2}} d\theta \int_{-\xi - \frac{\pi}{2}}^{-\xi + \frac{\pi}{2}} \cos(\phi + \xi) \cos^2 \theta d\phi}, \quad (14)$$

where a is the planet radius and d is the distance between the observer and planetary system. We express thermal phase curves either in terms of the planet-to-star flux ratio F_p/F_* , or using the planet's effective brightness temperature.

We define the observable signal for a planet's phase curve as the difference between the maximum and minimum flux (although a shift in the phase curve is another observable signal, see below), computed as

$$\text{Signal} = \left(\frac{a_p}{a_*} \right)^2 \frac{\int_{\lambda_1}^{\lambda_2} [\max(I_{p,\lambda}(\xi)) - \min(I_{p,\lambda}(\xi))] d\lambda}{\int_{\lambda_1}^{\lambda_2} B_{*,\lambda} d\lambda}, \quad (15)$$

where a_p and a_* are the radius of planet and star, respectively, (λ_1, λ_2) is the telescope bandpass over which we average, F_* is the flux from the host star (assumed to emit as a blackbody), and B_* is the intensity or brightness of the star.

To model the observational noise, we assume photon noise. Recent JWST observations with the MIRI Low-Resolution Spectrometer indicate a noise floor of at most ~ 25 ppm (Bouwman et al. 2023); this is less than the $\mathcal{O}(1000)$ ppm signal for atmospheric detection and the $\mathcal{O}(100)$ ppm signal for atmospheric characterization of white dwarf planets. The flux from the planetary system is dominated by the star (Cowan et al. 2015), so the observed number of photons equals

$$N_{\text{photon}} = \frac{\pi \tau \Delta t}{hc} \left(\frac{a_* D}{2d} \right)^2 \int_{\lambda_1}^{\lambda_2} B_*(\lambda) \lambda d\lambda, \quad (16)$$

where τ is telescope throughput, Δt is the integration time, D is the telescope diameter, and B_* is the star's flux, which we assume follows Planck's law. In the Poisson limit of large N_{photon} , the 1σ precision is approximately $\sqrt{\frac{2}{N_{\text{photon}}}}$, where the factor of $\sqrt{2}$ originates from the fact that the phase curve amplitude is measured as the difference between two flux

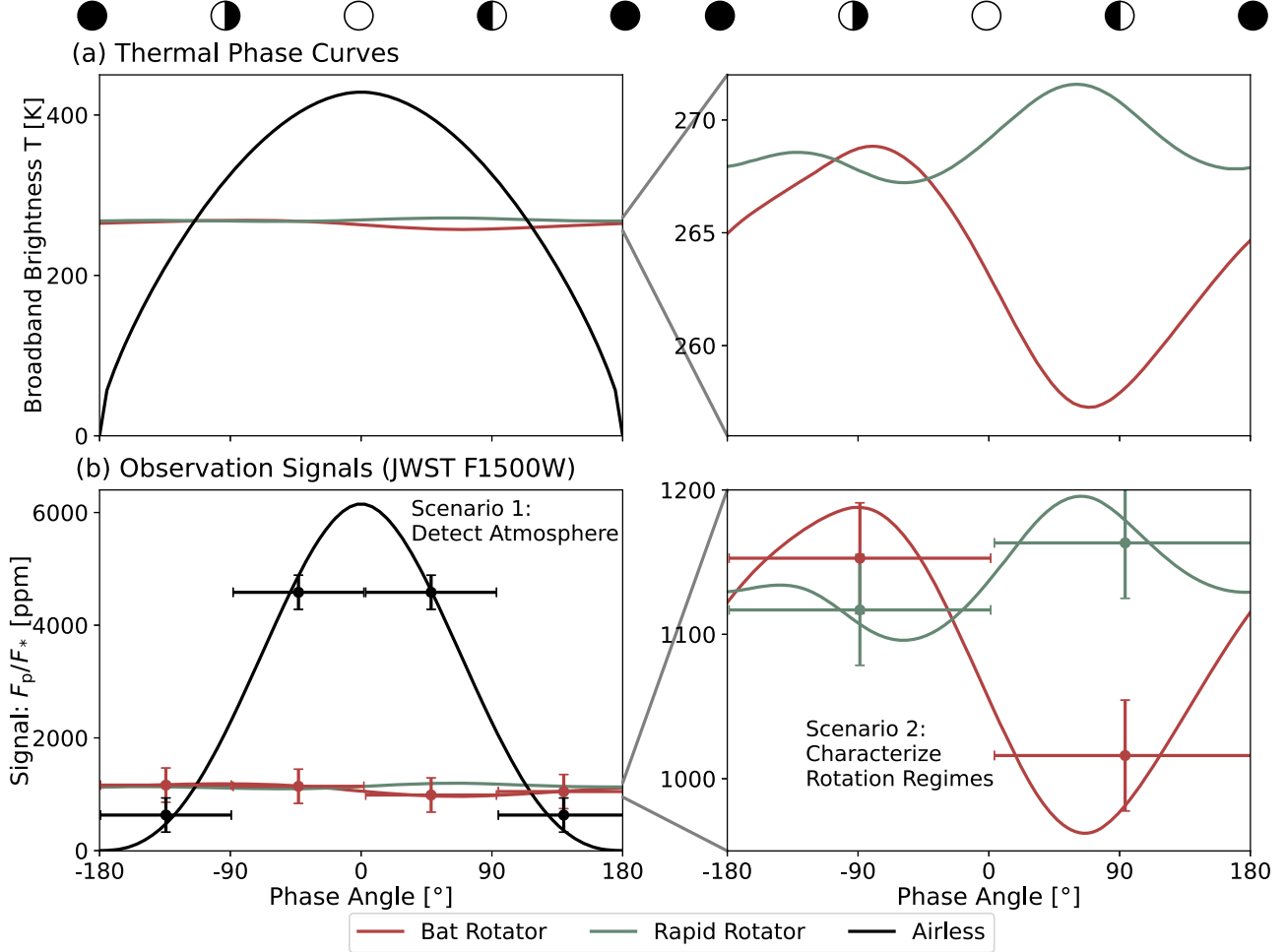


Figure 11. (a) Thermal phase curves of a bat rotator, a rapid rotator, and an airless planet, shown as $15\ \mu\text{m}$ brightness temperatures. (b) Observable signals compared to photon noise estimate; error bars show 1σ photometric precision with JWST MIRI F1500W. Scenario 1 (“Detect Atmosphere”) assumes a white dwarf at 25 pc and 3 hr per exposure. Scenario 2 (“Characterize Rotation Regimes”) assumes a white dwarf at 10 pc and 6 hr per exposure. The bat rotator and the rapid rotator are configured the same as in Figure 3. The phase curves of the bat rotator and the rapid rotator are based on GCM simulations and Equation (14); for the airless planet we assume zero albedo.

measurements (Equation (15)). The signal-to-noise ratio for thermal phase curves of temperate planets is highest in the mid-infrared, so we assume observations are performed with JWST MIRI F1500W (i.e., at $15\ \mu\text{m}$). For the white dwarf we assume an effective temperature of 10,000 K and the same stellar radius as in the GCM calculations ($a = 0.012\ a_{\odot}$).

We consider three planetary scenarios: an atmosphere-less blackbody planet, a rapid rotator, and a bat rotator. The latter two are both habitable and host a 1 bar $\text{N}_2\text{-H}_2\text{O}$ atmosphere, with their climates and phase curves simulated by the GCM (to simplify the comparison we use the two idealized simulations with identical stellar flux from Figure 3). Figure 11(a) shows the three planet scenarios result in very different phase curves. The airless planet has a large phase curve amplitude and is symmetric about the secondary eclipse (phase angle of 0°). In comparison, the two atmospheric scenarios have phase curves that are almost flat compared to the airless planet, due to the atmosphere’s effective day–night heat redistribution.

Zooming in on the difference between bat and rapid rotators, we find that they exhibit opposite phase shifts (Figure 11(a)). The rapid rotator’s phase curve maximum occurs after secondary eclipse, consistent with the fact that its equatorial cloud-free region is west of the SP (see Figure 3 and

Haqq-Misra et al. 2018). In contrast, the bat rotator’s phase curve maximum occurs before secondary eclipse, consistent with the fact that its equatorial cloud-free region is east of the SP (Figure 3). Bat rotators can thus be distinguished from rapid rotators based on their hot spot offsets.

How long would it take to measure these differences with JWST? Figure 11(b) shows two observing scenarios. Scenario 1 “Detect Atmosphere” assumes the system is 25 pc away, the same distance as WD 1856+534 b, which is the closest known transiting (giant) planet around a white dwarf (Vanderburg et al. 2020). For a bat rotator on a 12 hr orbit, a single JWST phase curve (12 hr total observation time, binned into four data points) can measure the phase curve amplitude of an airless planet with $>10\sigma$ confidence. That is sufficient to confidently distinguish between no atmosphere and a thick atmosphere. Scenario 2 “Characterize Rotation Regimes” assumes a more optimistic target at 10 pc. Although 10 pc is closer than any currently known transiting planet around a white dwarf, JWST might also be able to measure phase curves of nontransiting planets around white dwarfs (Limbach et al. 2022), which should greatly increase the number of nearby accessible targets. In this case five stacked phase curves of the bat rotator (60 hr total observation time, binned into two data points) would be sufficient to measure

the phase curve amplitude of the bat rotator with 3σ confidence. That is sufficient to characterize the bat rotator's hot spot offset, and distinguish between a bat rotator and rapid rotator. This observational effort is significantly less than that required to characterize habitable M dwarf planets such as the TRAPPIST-1 planets (Lustig-Yaeger et al. 2019). It arises because white dwarfs are much smaller than M dwarfs, significantly boosting the planet-to-star flux ratio and thus the observable signal (see Equation (15) and Kaltenegger et al. 2020). Overall, habitable white dwarf planets are thus attractive targets for characterization via thermal phase curves.

6. Conclusions

To summarize, we utilize a 3D GCM to investigate the inner edge of the habitable zone around white dwarfs. Since white dwarfs are compact and have low luminosity, habitable planets around them are likely tidally locked and rotate rapidly, with orbital periods ranging from a few hours to several days. We investigate the atmospheric dynamics of habitable tidally locked planets at such high rotation rates, and their implication for the habitable zone around white dwarfs. Our key results are as follows.

1. Our GCM simulations show habitable white dwarf planets with ultrashort orbital periods ($P \lesssim 1$ day) enter a new atmospheric dynamics regime that is distinct from atmospheric dynamics regimes on more slowly rotating tidally locked planets around main-sequence stars (Haqq-Misra et al. 2018). We name this regime the bat rotation regime due to its characteristic surface temperature pattern. On bat rotators the hottest surface temperatures move off the equator into the midlatitudes, while mean equatorial winds reverse sign from superrotation to subrotation.
2. The transition from rapid rotators to bat rotators at $P \sim 1$ day suggestively matches the transition from on-equator to off-equator hot spots in the linearized shallow water equations at $P \sim \mathcal{O}(1)$ day. Future work is needed to understand the transition in detail, which in the GCM is abrupt and likely involves nonlinear feedbacks. Our results also suggest the bat rotation state might not be accessible to hot Jupiters.
3. In the GCM, the transition to bat rotation increases the dayside cloud cover, which pushes the RGHL closer to the star. In addition, bat rotators have dayside anti-Hadley cells and weak vertical water transport, which lead to extremely dry upper atmospheres, allowing most white dwarf planets to avoid the moist greenhouse. As a result, the white dwarf habitable zone based on our GCM calculations is 50%–60% wider in instellation space than the habitable zone estimated based on 1D models.
4. For white dwarfs older than 3 Gyr, the bat rotation regime overlaps with most of the habitable zone. Many or most habitable white dwarf planets should thus be bat rotators.
5. Habitable white dwarf planets are attractive targets for characterization via JWST thermal phase curves. For a white dwarf at 25 pc, 12 hr (one full phase curve) should be sufficient to distinguish a thick atmosphere from an airless planet. For a white dwarf at 10 pc, 60 hr (multiple stacked phase curves) should be sufficient to distinguish between a bat rotator and a rapid rotator.

Acknowledgments

We thank Eric T. Wolf for developing ExoCAM and making it publicly available. We are grateful to Jun Yang, Tad Komacek, Xianyu Tan, Lixiang Gu, Xinyi Song, and Xintong Lyu for helpful comments. We thank Aomawa Shields and Pier-Emmanuel Tremblay for sharing white dwarf SEDs. D.D.B.K. acknowledges support from the National Natural Science Foundation of China (NSFC) under grant 42250410318. The simulation outputs used to make figures and tables in this study are available on Zenodo at doi:10.5281/zenodo.11242931 (Zhan et al. 2024).

Appendix A Sensitivity Test

A.1. White Dwarf Spectra Energy Distribution

As discussed in Section 2, our white dwarf SEDs are either from ExoCAM or based on the 3D non-LTE models presented in Tremblay et al. (2013, 2015).⁶ We find that the exact choice of white dwarf SED has a small but nonzero influence on GCM output.

Figure 12 shows a sensitivity test for an 8000 K white dwarf. The top row shows the different SEDs, while the bottom row shows the resulting GCM surface temperature maps. We find a moderate difference in the global-mean surface temperature: 287.0 K with the 3D non-LTE model SED versus 282.4 K with the default ExoCAM SED. In addition, Figure 12 shows that the pattern of surface temperature is highly similar between both cases. To be more consistent with other studies that use ExoCAM, we therefore choose to use ExoCAM SEDs whenever possible, and 3D non-LTE model SEDs when there are no ExoCAM SEDs provided (i.e., for 3500 K and 6500 K white dwarfs).

A.2. Horizontal Resolution

The Rossby deformation radius, a fundamental length scale for atmospheric dynamics, is smaller on planets with higher rotation rates. We therefore investigate whether the horizontal resolution in ExoCAM is adequate for rapidly rotating planets.

We consider two white dwarf planets with orbital periods of about 10 hr and 4 hr. Each case is simulated using two different horizontal resolutions, $4^\circ \times 5^\circ$ (corresponding to Δx about $450 \text{ km} \times 550 \text{ km}$ at the equator) and $1.9^\circ \times 2.5^\circ$ (Δx about $200 \text{ km} \times 250 \text{ km}$ at the equator). For the more slowly rotating planet, the $4^\circ \times 5^\circ$ resolution is significantly smaller than the equatorial Rossby deformation radius, $L_{Ro} \sim 5\Delta x$, while for the more rapidly rotating planet the $4^\circ \times 5^\circ$ resolution is comparable to the Rossby deformation radius, $L_{Ro} \sim 2\Delta x$.

Figure 13 shows global-mean vertical temperature profiles of the simulations with different horizontal resolutions. We find that, with an orbital period of about 10 hr, increasing the horizontal resolution only has a minor impact on the atmospheric temperature structure; temperatures in the upper atmosphere change by about 10 K while temperatures near the surface are essentially the same. However, with a shorter orbital period of about 4 hr, increasing the resolution has a much bigger impact; temperatures in the upper atmosphere change by more than 100 K while temperatures near the surface change by around 5 K. Our results are qualitatively consistent with the ExoCAM results from Wei et al. (2020), who

⁶ <https://warwick.ac.uk/fac/sci/physics/research/astro/people/tremblay/modelgrids>

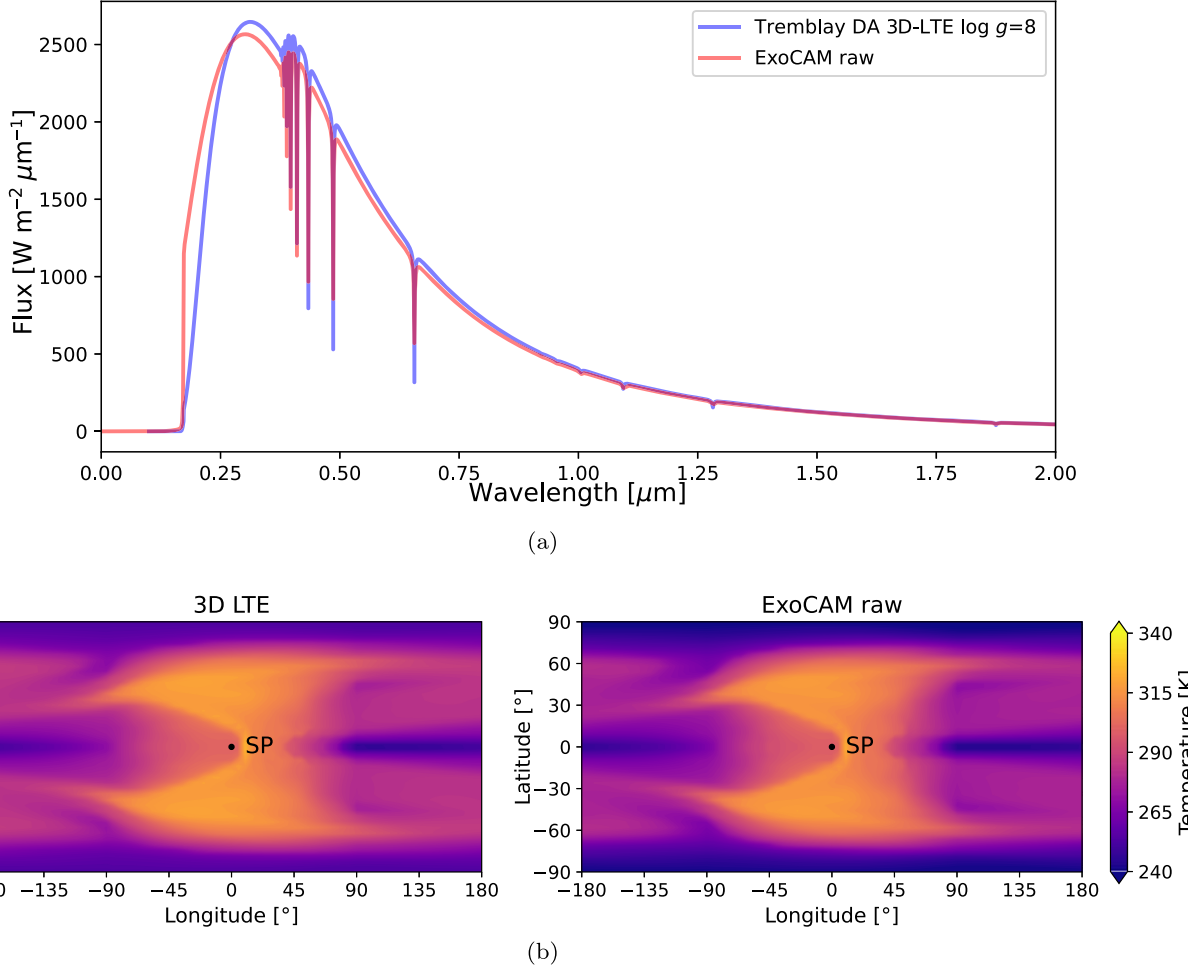


Figure 12. (a) Two similar SEDs for an 8000 K white dwarf. The red line shows the default SED from ExoCAM, while the blue line shows an SED based on a 3D non-LTE model (DA spectral type, stellar surface gravity about 10^{10} m s^{-2}). (b) Surface temperature maps, simulated with ExoCAM. Both simulations are identical except for the stellar SED.

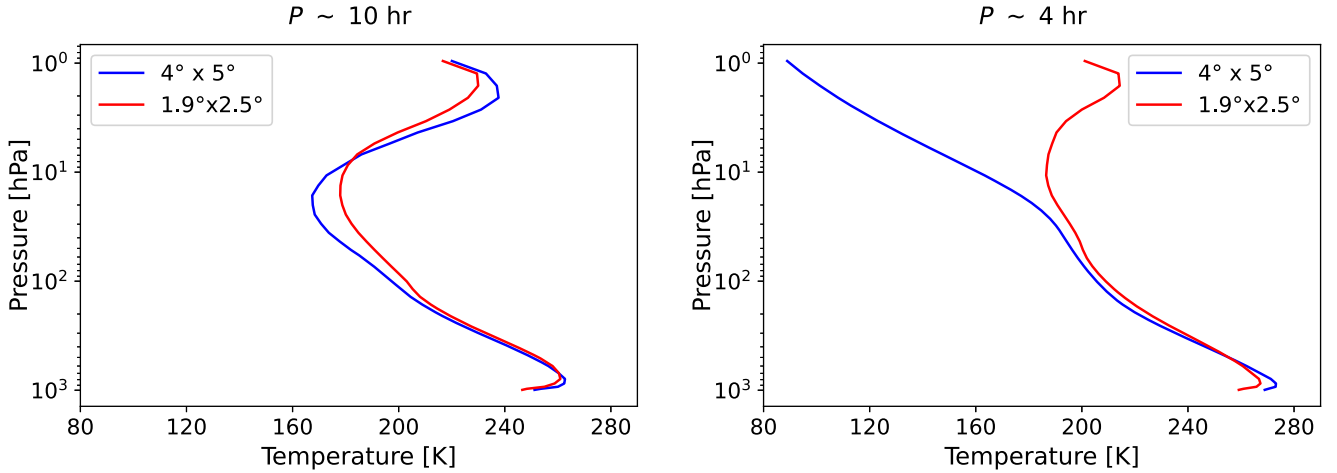


Figure 13. Sensitivity test on the impact of ExoCAM horizontal resolution. Both panels show global-mean vertical temperature profiles of white dwarf planets receiving the same insolation as Earth. Left panel: 5000 K white dwarf. Right panel: 3500 K white dwarf. The blue lines show lower resolution ($4^\circ \times 5^\circ$), and the red lines show higher resolution ($1.9^\circ \times 2.5^\circ$).

found that simulations with higher resolution result in drier, warmer upper atmospheres and cooler surfaces. However, Wei et al. (2020) only reported a small sensitivity to changes in horizontal resolution, whereas in some of our simulations the

sensitivity is large (see Figure 13, right panel). This is presumably because we are considering much more rapidly rotating planets; the shortest orbital period in Wei et al. (2020) was 4.25 days, whereas here we consider orbital periods down to a few hours.

In our GCM simulations we therefore use a resolution of either $4^\circ \times 5^\circ$ or $1.9^\circ \times 2.5^\circ$, as shown in Table 1. We do not use resolutions higher than $1.9^\circ \times 2.5^\circ$ because Figure 13 (left panel) suggests that, once the Rossby deformation radius is much larger than the grid scale, any further increase in the horizontal resolution does not lead to significant changes in the simulated climate.

Appendix B Simulation Details

B.1. Tables

The following tables show model configuration (Table 1) and key output quantities (Table 2) from all our simulations.

Table 1
Configuration of the Global Climate Model Simulations in This Work

T_{WD} (K)	F_p/F_\oplus	Orbital Period (day)	Horizontal Resolution	Rotation Regime
3500	1.0	0.1474	$1.9^\circ \times 2.5^\circ$	bat
	1.2	0.1286	$1.9^\circ \times 2.5^\circ$...
	1.3	0.1211	$1.9^\circ \times 2.5^\circ$	(crash)
5000	1.0	0.4299	$4^\circ \times 5^\circ$	bat
	1.2	0.3749	$4^\circ \times 5^\circ$	bat
	1.3	0.3531	$4^\circ \times 5^\circ$	bat
	1.35	0.3432	$4^\circ \times 5^\circ$	bat
	1.4	0.3340	$4^\circ \times 5^\circ$	(crash)
6500	1.0	0.9444	$4^\circ \times 5^\circ$...
	1.417	0.7272	$4^\circ \times 5^\circ$	bat
	1.5	0.6968	$4^\circ \times 5^\circ$	bat
	1.621	0.6574	$4^\circ \times 5^\circ$	bat
	1.7	0.6343	$4^\circ \times 5^\circ$	(crash)
8000	1.0	1.7606	$4^\circ \times 5^\circ$	rapid
	1.417	1.3557	$4^\circ \times 5^\circ$	rapid
	1.519	1.2868	$4^\circ \times 5^\circ$	rapid
	1.621	1.2256	$4^\circ \times 5^\circ$	rapid
	1.723	1.1708	$4^\circ \times 5^\circ$	rapid
	1.965	1.0609	$4^\circ \times 5^\circ$	bat
	2.02	1.0391	$4^\circ \times 5^\circ$	bat
	2.12	1.0021	$4^\circ \times 5^\circ$	bat
	2.17	0.9848	$4^\circ \times 5^\circ$	(crash)
	1.0	3.4389	$4^\circ \times 5^\circ$	rapid
10,000	1.929	2.1009	$4^\circ \times 5^\circ$	rapid
	2.12	1.9573	$4^\circ \times 5^\circ$	rapid
	2.17	1.9234	$4^\circ \times 5^\circ$	rapid
	2.22	1.8908	$4^\circ \times 5^\circ$	rapid
	2.27	1.8595	$4^\circ \times 5^\circ$	(crash)

Table 2
Key Output Quantities for the Global Climate Model Simulations in This Work

T_{WD} (K)	F_p/F_\oplus	T_s (K)	TOA Net SW (W m^{-2})	TOA Net LW (W m^{-2})	Planetary Albedo	Rotation Regime
3500	1.0	259.60	206.85	209.05	0.3918	bat
	1.2	308.60	281.76	280.35	0.3096	...
	1.3	(crash)
5000	1.0	252.03	194.66	197.00	0.4273	bat
	1.2	273.34	232.01	233.36	0.4311	bat
	1.3	288.51	259.16	258.93	0.4135	bat
	1.35	309.36	292.96	290.01	0.3615	bat
	1.4	(crash)
6500	1.0	241.49	173.21	176.84	0.4904	...
	1.417	278.39	250.47	251.40	0.4799	bat
	1.5	288.86	269.66	269.35	0.4711	bat
	1.621	309.21	302.83	302.12	0.4504	bat
	1.7	(crash)

Table 2
(Continued)

T_{WD} (K)	F_p/F_\oplus	T_s (K)	TOA Net SW (W m^{-2})	TOA Net LW (W m^{-2})	Planetary Albedo	Rotation Regime
8000	1.0	216.47	127.40	130.92	0.6251	rapid
	1.417	262.10	216.71	220.13	0.5499	rapid
	1.519	270.41	233.28	235.30	0.5481	rapid
	1.621	278.52	248.08	249.57	0.5496	rapid
	1.723	284.14	258.21	259.74	0.5590	rapid
	1.965	299.26	289.74	288.37	0.5661	bat
	2.02	308.85	305.72	304.82	0.5546	bat
	2.12	316.33	305.27	305.31	0.5762	bat
	2.17	(crash)
10,000	1.0	212.21	119.46	123.55	0.6484	rapid
	1.929	275.05	250.25	252.22	0.6182	rapid
	2.12	295.92	289.06	288.59	0.5987	rapid
	2.17	306.59	303.29	300.37	0.5886	rapid
	2.22	333.34	295.43	296.47	0.6080	rapid
	2.27	(crash)

Note. Quantities are computed based on 10 yr averages after simulations reach statistical equilibrium. Shown are top-of-atmosphere (TOA) long-wave (LW) and shortwave (SW) intensities.

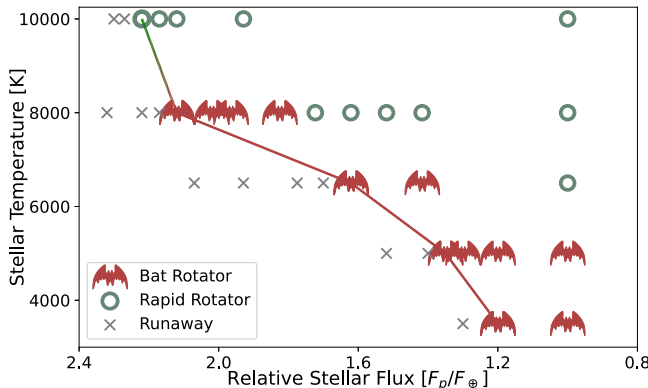


Figure 14. RGHL around white dwarfs. The bat patterns and green circles represent the bat rotators and the rapid rotators, respectively, which are converged simulations. The gray crosses are runaway simulations in our result.

B.2. Runaway Greenhouse Limit

Figure 14 and Table 1 show how we determine the RGHL. At each stellar temperature, the RGHL is equal to the insolation of the last simulation that still converges (second-to-last row in each T_{WD} block in Table 1). The crosses in Figure 14 show other simulations that also crashed.

Appendix C Appendix: Computing Thermal Flux

Here we rederive the formula for the observer-projected flux stated in Appendix C of Koll & Abbot (2015). Our derivation corrects a factor of R^2/d^2 which is missing from the expression in Koll & Abbot (2015); also note that the formula in Koll & Abbot (2015) is not area averaged, as it would otherwise be missing a factor of π . We additionally clarify the difference between flux and intensity: flux quantifies the amount of energy passing through a unit area per unit time, while intensity specifies the energy per unit area, time, and solid angle in a given direction. Our derivation below yields the same result as that obtained by Seager (2010).

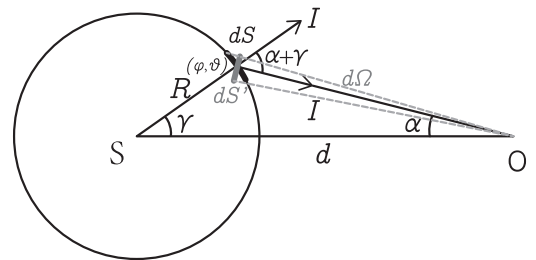


Figure 15. Sketch of a small area on a spherical planet, projected onto the observer's plane. dS : area element on the planet, located at (ϕ, θ) . dS' : projection of dS toward the observer. Points O and S represent the observer and the center of the spherical planet, respectively.

We assume the planet emits with isotropic intensity I . For any point (ϕ, θ) on the surface of the planet, a plane can be identified that passes through (ϕ, θ) , the center of the planet, and the observer. We then project onto this plane, as shown in Figure 15. The angles γ and α are related to ϕ and θ via

$$\cos \gamma = \cos \phi \cos \theta, \quad (C1)$$

$$\sin \alpha = R \frac{\sin(\alpha + \gamma)}{d}. \quad (C2)$$

Next we consider the solid angle $d\Omega$, which denotes how large a surface area on the sphere at (ϕ, θ) , $dS = R^2 \cos \theta d\theta d\phi$, appears to the observer. The projection of the surface area dS in the direction of the solid angle is dS' , and the angle between dS and dS' is $\alpha + \gamma$, so

$$dS' = dS \cos(\alpha + \gamma) = R^2 \cos \theta d\theta d\phi \cos(\alpha + \gamma). \quad (C3)$$

According to the law of sines, the solid angle can be written as

$$d\Omega = \frac{dS'}{d^2} \left(\frac{\sin(\alpha + \gamma)}{\sin \gamma} \right)^2. \quad (C4)$$

Here α is the angle between $d\Omega$ and the direction of the observer. Assuming $d \gg R$ and $\lim \alpha \rightarrow 0$, we get $\cos \alpha \rightarrow 1$, $\sin(\alpha + \gamma) = \sin \alpha \cos \gamma + \cos \alpha \sin \gamma \rightarrow \sin \gamma$, and $\cos(\alpha + \gamma) = \cos \alpha \cos \gamma - \sin \alpha \sin \gamma \rightarrow \cos \gamma$. To derive the net flux

received at distance d by the observer, we integrate over the hemisphere facing the observer

$$\begin{aligned} F_{\text{obs}} &= \int I \cos \alpha d\Omega \\ &= \int_{-\frac{\pi}{2}}^{\frac{\pi}{2}} \int_{-\frac{\pi}{2}}^{\frac{\pi}{2}} I(\phi, \theta) \cdot 1 \cdot \frac{\cos \gamma R^2 \cos \theta d\theta d\phi}{d^2} \\ &= \frac{R^2}{d^2} \int_{-\frac{\pi}{2}}^{\frac{\pi}{2}} \int_{-\frac{\pi}{2}}^{\frac{\pi}{2}} I(\phi, \theta) \cos \phi \cos^2 \theta d\theta d\phi \\ &= \frac{\pi R^2}{d^2} \frac{\int_{-\frac{\pi}{2}}^{\frac{\pi}{2}} d\theta \int_{-\frac{\pi}{2}}^{\frac{\pi}{2}} I(\phi, \theta) \cos \phi \cos^2 \theta d\phi}{\int_{-\frac{\pi}{2}}^{\frac{\pi}{2}} d\theta \int_{-\frac{\pi}{2}}^{\frac{\pi}{2}} \cos \phi \cos^2 \theta d\phi}. \end{aligned} \quad (C5)$$

ORCID iDs

Rui Zhan <https://orcid.org/0009-0005-4936-7289>
 Daniel D. B. Koll <https://orcid.org/0000-0002-9076-6901>
 Feng Ding <https://orcid.org/0000-0001-7758-4110>

References

- Agol, E. 2011, *ApJL*, 731, L31
 Barnes, R., & Heller, R. 2013, *AsBio*, 13, 279
 Becker, J., Seligman, D. Z., Adams, F. C., & Styczinski, M. J. 2023, *ApJL*, 945, L24
 Bouwman, J., Kendrew, S., Greene, T. P., et al. 2023, *PASP*, 135, 038002
 Bédard, A., Bergeron, P., Brassard, P., & Fontaine, G. 2020, *ApJ*, 901, 93
 Charnay, B., Meadows, V., Misra, A., Leconte, J., & Arney, G. 2015, *ApJ*, 813, L1
 Cohen, M., Palmer, P. I., Paradise, A., Bollasina, M. A., & Tiranti, P. I. 2024, *AJ*, 167, 97
 Cortes, J., & Kipping, D. M. 2019, *MNRAS*, 488, 1695
 Cowan, N. B., & Agol, E. 2008, *ApJ*, 678, L129
 Cowan, N. B., Voigt, A., & Abbot, D. S. 2012, *ApJ*, 757, 80
 Cowan, N. B., Greene, T., Angerhausen, D., et al. 2015, *PASP*, 127, 311
 Del Genio, A. D., Way, M. J., Amundsen, D. S., et al. 2019, *AsBio*, 19, 99
 Doshi, D., Cowan, N. B., & Huang, Y. 2022, *MNRAS*, 515, 1982
 Farihi, J. 2016, *NewAR*, 71, 9
 Farihi, J., Hermes, J. J., Marsh, T. R., et al. 2022, *MNRAS*, 511, 1647
 Fontaine, G., Brassard, P., & Bergeron, P. 2001, *PASP*, 113, 409
 Fujii, Y., Del Genio, A. D., & Amundsen, D. S. 2017, *ApJ*, 848, 100
 Fusillo, N. P. G., Tremblay, P.-E., Cukanovaite, E., et al. 2021, *MNRAS*, 508, 3877
 Gill, A. E. 1980, *QJRMS*, 106, 447
 Golovin, A., Reffert, S., Just, A., et al. 2023, *A&A*, 670, A19
 Gordon, I., Rothman, L., Hill, C., et al. 2017, *JQSRT*, 203, 3
 Haqq-Misra, J., Wolf, E. T., Joshi, M., Zhang, X., & Kopparapu, R. K. 2018, *ApJ*, 852, 67
 Held, I. M., & Suarez, M. J. 1994, *BAMS*, 75, 1825
 Hu, Y., & Yang, J. 2014, *PNAS*, 111, 629
 Jiménez-Esteban, F. M., Torres, S., Rebassa-Mansergas, A., et al. 2018, *MNRAS*, 480, 4505
 Kaltenegger, L., MacDonald, R. J., Kozakis, T., et al. 2020, *ApJL*, 901, L1
 Kaspi, Y., & Showman, A. P. 2015, *ApJ*, 804, 60
 Kasting, J. F., Whitmire, D. P., & Reynolds, R. T. 1993, *Icar*, 101, 108
 Kiladis, G. N., Wheeler, M. C., Haertel, P. T., Straub, K. H., & Roundy, P. E. 2009, *RvGeo*, 47, RG2003
 Koester, D., Gänsicke, B. T., & Farihi, J. 2014, *A&A*, 566, A34
 Koll, D. D. B. 2022, *ApJ*, 924, 134
 Koll, D. D. B., & Abbot, D. S. 2015, *ApJ*, 802, 21
 Koll, D. D. B., & Komacek, T. D. 2018, *ApJ*, 853, 133
 Koll, D. D. B., Malik, M., Mansfield, M., et al. 2019, *ApJ*, 886, 140
 Komacek, T. D., & Abbot, D. S. 2019, *ApJ*, 871, 245
 Kopparapu, R. K., Wolf, E. T., Arney, G., et al. 2017, *ApJ*, 845, 5
 Kopparapu, R. K., Wolf, E. T., Haqq-Misra, J., et al. 2016, *ApJ*, 819, 84
 Kopparapu, R. K., Ramirez, R., Kasting, J. F., et al. 2013, *ApJ*, 765, 131
 Kozakis, T., Lin, Z., & Kaltenegger, L. 2020, *ApJ*, 894, L6
 Leconte, J., Forget, F., Charnay, B., et al. 2013, *A&A*, 554, A69
 Limbach, M. A., Vanderburg, A., Stevenson, K. B., et al. 2022, *MNRAS*, 517, 2622
 Lin, Z., Seager, S., Ranjan, S., Kozakis, T., & Kaltenegger, L. 2022, *ApJL*, 925, L10
 Lissauer, J. J., & de Pater, I. 2019, *Fundamental Planetary Science: Physics, Chemistry and Habitability* (Cambridge: Cambridge Univ. Press)
 Lustig-Yaeger, J., Meadows, V. S., & Lincowski, A. P. 2019, *AJ*, 158, 27
 Malik, M., Kempton, E. M.-R., Koll, D. D. B., et al. 2019, *ApJ*, 886, 142
 Mansfield, M., Kite, E. S., Hu, R., et al. 2019, *ApJ*, 886, 141
 Meadows, V. S., Lincowski, A. P., & Lustig-Yaeger, J. 2023, *PSJ*, 4, 192
 Merlis, T. M., & Schneider, T. 2010, *JAMES*, 2, 13
 Morley, C. V., Kreidberg, L., Rustamkulov, Z., Robinson, T., & Fortney, J. J. 2017, *ApJ*, 850, 121
 Muñoz, D. J., & Petrovich, C. 2020, *ApJL*, 904, L3
 Neale, R. B., Chen, C.-C., Gettelman, A., et al. 2010, NCAR Tech. Note NCAR/TN-486, STR 1
 Noda, S., Ishiwatari, M., Nakajima, K., et al. 2017, *Icar*, 282, 1
 O'Connor, C. E., Liu, B., & Lai, D. 2020, *MNRAS*, 501, 507
 Penn, J., & Vallis, G. K. 2018, *ApJ*, 868, 147
 Perna, R., Menou, K., & Rauscher, E. 2010, *ApJ*, 719, 1421
 Pierrehumbert, R., & Gaidos, E. 2011, *ApJ*, 734, L13
 Putirka, K. D., & Xu, S. 2021, *NatCo*, 12, 6168
 Seager, S. 2010, *Exoplanet Atmospheres* (Princeton: Princeton Univ. Press)
 Selsis, F., Wordsworth, R. D., & Forget, F. 2011, *A&A*, 532, A1
 Showman, A. P., & Kaspi, Y. 2013, *ApJ*, 776, 85
 Showman, A. P., & Polvani, L. M. 2011, *ApJ*, 738, 71
 Tremblay, P.-E., Gianninas, A., Kilic, M., et al. 2015, *ApJ*, 809, 148
 Tremblay, P.-E., Ludwig, H.-G., Steffen, M., & Freytag, B. 2013, *A&A*, 559, A104
 Turbet, M., Fauchez, T. J., Sergeev, D. E., et al. 2022, *PSJ*, 3, 211
 Vallis, G. K. 2017, *Atmospheric and Oceanic Fluid Dynamics: Fundamentals and Large-Scale Circulation* (2nd ed.: Cambridge: Cambridge Univ. Press)
 Vanderburg, A., Rappaport, S. A., Xu, S., et al. 2020, *Natur*, 585, 363
 Veras, D. 2016, *RSOS*, 3, 150571
 Veras, D. 2021, *oeps book*, 1, 1
 Veras, D., & Gaensicke, B. T. 2015, *MNRAS*, 447, 1049
 Wei, M., Zhang, Y., & Yang, J. 2020, *ApJ*, 898, 156
 Winn, J. N., Sanchis-Ojeda, R., & Rappaport, S. 2018, *NewAR*, 83, 37
 Wolf, E. T., Kopparapu, R., Haqq-Misra, J., & Fauchez, T. J. 2022, *PSJ*, 3, 7
 Wolf, E. T., Shields, A. L., Kopparapu, R. K., Haqq-Misra, J., & Toon, O. B. 2017, *ApJ*, 837, 107
 Wolf, E. T., & Toon, O. B. 2014, *GeoRL*, 41, 167
 Wu, Z., Sarachik, E., & Battisti, D. 2001, *JAS*, 58, 724
 Yang, J., Abbot, D. S., Koll, D. D. B., Hu, Y., & Showman, A. P. 2019, *ApJ*, 871, 29
 Yang, J., Boué, G., Fabrycky, D. C., & Abbot, D. S. 2014, *ApJ*, 787, L2
 Yang, J., Cowan, N. B., & Abbot, D. S. 2013, *ApJ*, 771, L45
 Yang, J., Zhang, Y., Fu, Z., et al. 2023, *NatAs*, 7, 9
 Zhan, R., Koll, D., & Ding, F. 2024, *Novel Atmospheric Dynamics Shape Inner Edge of Habitable Zone Around White Dwarfs [Dataset]*, v1, Zenodo, doi:10.5281/zenodo.11242931
 Zhang, Y., & Yang, J. 2020, *ApJ*, 901, L36